

Journal of Geophysical Research, 100, 13,951–13,966, 1995

Stratospheric trace constituents simulated by a three-dimensional general circulation model: Comparison with UARS data

Richard S. Eckman, William L. Grose, Richard E. Turner, W. Thomas Blackshear, and James M. Russell III

NASA Langley Research Center, Hampton, Virginia

Lucien Froidevaux and Joe W. Waters

Jet Propulsion Laboratory, Pasadena, California

J. B. Kumer and Aidan E. Roche

Lockheed Palo Alto Research Laboratory, Palo Alto, California

Abstract

Constituent distributions are presented from the NASA Langley three-dimensional general circulation model, incorporating a comprehensive chemistry scheme. A 7-year, gas phase model simulation was performed to investigate long-term model stability. In addition, a 1-year simulation was made using parameterized polar heterogeneous processes and reactions occurring on sulfate aerosols. The results of these simulations are compared with species climatologies and with satellite data sets in order to characterize and evaluate model performance and identify aspects of the chemical scheme requiring improvement. The agreement between the modeled seasonal variation of total ozone and the measurement climatologies is satisfactory but with some differences with respect to the depth and persistence of the southern springtime ozone depletion. Comparisons of the model simulation with observations made from UARS were performed. There is good accord between the microwave limb sounder observations of ozone and the model. Areas of agreement and disagreement are revealed between the model and the cryogenic array etalon spectrometer measurements of HNO_3 and ClONO_2 , suggesting the need for a more detailed representation of sulfate aerosol processes in the model. The comparison between the modeled and the measured partitioning of odd chlorine species is improved in the upper stratosphere by the inclusion of an additional pathway to HCl from the reaction of $\text{ClO} + \text{OH}$.

Introduction

The possible impact of perturbations to the ozone layer has stimulated significant research in the subject for over two decades. Much work has been done on simulating the distribution of stratospheric ozone and other trace constituents using numerical models of the chemistry and dynamics of the middle atmosphere. Computational expense dictates that simplifying assumptions must be made because the numerical representations of the chemical, radiative, and dynamical characteristics of the atmosphere are complex. For this reason, two-dimensional models have been used extensively [e.g., *World Meteorological Organization (WMO)*, 1988] to simulate the present-day atmosphere as well as historical and future changes to ozone resulting from both natural and anthropogenic perturbations. But given their two-dimensional nature, such models are often not able to properly simulate inherently three-dimensional processes except in an ad hoc manner. Examples include the polar vortex isolation plus its role in the depletion of Antarctic ozone and the dispersion of emissions from a fleet of high-speed aircraft flying in the lower stratosphere [e.g., *WMO*, 1991; *Stolarski and Wesoky*, 1993].

An early study, coupling chemistry to a global general circulation model (GCM) by *London and Park* [1974], examined the ozone budget in an oxygen-hydrogen-nitrogen chemical framework. Continuing enhancements in computer technology now permit simulations using GCMs which incorporate extensive chemical schemes. *Kaye and Rood* [1989] examined the relative importance of chemistry and transport on the partitioning of total chlorine. More recent studies by *Chipperfield et al.* [1993] and *Lefèvre et al.* [1994] utilized three-dimensional chemistry-transport models to examine the morphology of trace gases for short time periods during disturbed wintertime conditions in the northern hemisphere. *Lary et al.* [1994] used a three-dimensional model to examine nitrogen chemistry for a perturbed period in the northern hemisphere during the winter of 1987.

The NASA Langley Research Center three-dimensional GCM and chemistry-transport model (CTM) has been undergoing continuous development for over a decade and now has the capability of performing simulations using a chemistry package to model 40 trace stratospheric constituents. The CTM utilizes winds and temperatures calculated by the free-running GCM. As a result, the model is generally not used in the mode of simulating a specific time period. Rather, it is used to study the interactions among radiative, chemical, and dynamical processes and to conduct long-term simulations for application to global

change studies. *Chipperfield et al.* [1993] point out the inherent importance of model initialization on the results of short-term integrations. Given the capability to run simulations for multiple years on single processor workstations at modest wavenumber resolution, our model results are less dependent on imperfectly known initial conditions or the actual methods of initialization.

This paper describes the chemistry-transport module and reports on some recent multiyear experiments with a variety of chemical scenarios. The baseline (“control”) simulation uses only gas phase chemistry. Other simulations were run which include a parameterization of polar heterogeneous processes and processes on sulfate aerosols. We show comparisons with UARS measurements during several time periods, concentrating on a period during which constituent validation studies were performed and also during southern hemisphere springtime. The impetus is manifold: to evaluate the model’s chemical scheme and interpret areas of agreement and disagreement with observation, to investigate whether UARS measurements can place useful constraints on the model using variant chemical processes, and to identify model mechanisms and parameterizations that require improvement.

The paper is organized as follows: The following section describes the chemistry-transport module of the NASA Langley three-dimensional model. The results of a multiyear model simulation with gas phase chemistry and a 1-year simulation incorporating polar heterogeneous processes and sulfate aerosol chemistry are then presented. We look at the seasonal evolution of several key species by comparing with available climatologies and observations. We then focus on the chlorine family, comparing the model with UARS measurements during southern hemisphere springtime. The final section summarizes the results and outlines plans for model enhancements.

Model Description

The NASA Langley general circulation model has been described in previous publications [*Grose et al.*, 1987; *Blackshear et al.*, 1987; *Pierce et al.*, 1993]. Briefly, the model is global in domain and uses a spectral representation of the dependent variables in the horizontal dimension with triangular truncation (zonal wavenumber 16 (T16), in this version) of the spherical harmonic expansions. A second-order, centered finite difference approximation is employed in the vertical dimension. Time integration is accomplished with a semi-implicit technique using a 30-min time step. Previous descriptions of the chemistry-transport model include *Grose et al.* [1990] and *Eckman et al.* [1993]. A more complete description of the

CTM, which has evolved substantially in recent years, is presented here.

The CTM spans the altitude range from the surface to approximately 60 km in 24 vertical levels. In the stratosphere there are 14 levels with a vertical resolution of approximately 3 km. A sigma coordinate system [Phillips, 1957] is employed which takes into account variations in surface orography. We use a grid of approximately 5.5° in latitude by 5.5° in longitude, so that the short waves in the Fourier decomposition are recovered exactly [e.g., Hoskins and Simmons, 1975]. The time step is 30 min using a leapfrog integration technique. The CTM is formulated essentially identical to the GCM with the exception of the time integration technique. The occurrence of negative mixing ratios is handled in the vertical by switching from central differencing to upstream differencing. The technique is mass-conserving and works if there are adjacent grid points with negative values [Grose *et al.*, 1987]. Mass conservation in the model was checked by a simulation with a passive tracer. The model conserved to greater than 99% over a 1-year run.

Fifteen chemical families or individual constituents are explicitly transported by the model. They are odd oxygen ($O_x=O + O(^1D) + O_3$), total odd nitrogen ($NO_y=N + NO + NO_2 + NO_3 + 2N_2O_5 + HNO_3 + HO_2NO_2 + ClONO_2$), HNO_3 , total inorganic chlorine ($Cl_y=Cl + ClO + HOCl + HCl + ClONO_2 + 2Cl_2 + 2Cl_2O_2$), N_2O_5 , H_2O_2 , HCl, $ClONO_2$, N_2O , $CFCl_3$, CF_2Cl_2 , CCl_4 , CH_3Cl , CH_3CCl_3 , and a proxy for condensed phase nitric acid, hereinafter denoted as nitric acid trihydrate (NAT). We make the ad hoc assumption that the NAT particles are small enough to be advected in the same manner as the gas phase constituents. Yet, the particles may also grow large enough to settle out of the atmosphere (see below). Odd hydrogen (HO_x) is assumed to be in photochemical equilibrium throughout the model domain. A simplified methane oxidation scheme is included through the representation of CH_x chemistry. The present version of the model does not contain bromine chemistry. Typically, a 1-day T16 simulation requires 12 min of computer time on a Digital Equipment Corporation 3000/400 alpha workstation.

Table 1 shows the 40 species which are considered in the model. Those not solved explicitly are obtained by partitioning the families using standard photochemical equilibrium techniques using 29 photolytic reactions (Table 2) and 87 chemical reactions (Table 3). Four of these species, H_2O , CH_4 , H_2 , and CO , are specified as a function of latitude, altitude, and time, using calculations from a two-dimensional model [Garcia and Solomon, 1982] above 16 km and joined with fields from the Max Planck Institute for Chemistry two-dimensional model in the troposphere

[Gidel *et al.*, 1983].

Photodissociation rates are obtained using a table lookup method to reduce computational time. The rates are stored as a function of slant column O_2 and O_3 density and, where appropriate, temperature. A comparison with detailed photolysis calculations shows satisfactory agreement with the approximate method employed here. At high solar zenith angles (above 60°) a Chapman function approximation is used to account for spherical geometry [Smith and Smith, 1972]. Neither the effects of multiple scattering nor the surface reflection are accounted for in the present version of the model. Absorption cross sections were obtained from DeMore *et al.* [1990] and Baulch *et al.* [1982]. The ultraviolet solar irradiances are derived from the recommendations of Frederick *et al.* [1986] based on satellite and rocket measurements.

Kinetic rates are taken from the compilation of DeMore *et al.* [1990]. Unlike the photolysis rate calculation, the bimolecular and termolecular rate constants are explicitly calculated at each time step. Unless otherwise specified, we include the reaction of $ClO + OH$ with a branching ratio of 5% to the $HCl + O_2$ channel, as suggested by Toumi and Bekki [1993] and in earlier work by McElroy and Salawitch [1989] and Natarajan and Callis [1991], to improve the agreement of modeled chlorine chemistry with observation. Production terms for the NO_y and Cl_y source gases are specified with constant surface mixing ratios taken from recommendations appropriate for 1990, originally formulated for use in two-dimensional assessment simulations [WMO, 1991].

At each time step, the chemical solution technique is as follows: Active nitrogen and active chlorine are obtained from the total odd nitrogen and total odd chlorine families, respectively, by subtracting out reservoir species. Initial partitioning of the oxygen, hydrogen, and nitrogen families is performed. Tests for photochemical equilibrium of $ClONO_2$, N_2O_5 , and HNO_3 are made. If any of these species are in photochemical equilibrium, they are added back into their respective families in subsequent partitioning calculations. An iterative approach is then used to partition the chlorine, nitrogen, and hydrogen families until convergence in the OH number density is reached. The convergence criterion is specified to be when the difference between OH calculations in the iterative loop is less than 0.01%. The chemical source and sink terms for each family or transported species are then calculated. These terms are used in the chemical time rate of change equations to perform the time integration.

The transport of the 15 families and species is performed using an "off-line" approach; that is, the wind and temperature fields generated by the GCM are used as in-

put into the set of mass continuity equations for the trace constituents in the CTM. In this case, there is no feedback between the calculated ozone and GCM-calculated temperatures. A fully coupled version of the model is currently in a development and testing phase.

For the described multiyear simulation the winds and temperatures from a 1-year GCM simulation are continuously repeated. The GCM flow fields (i.e., winds and temperatures) are interpolated during a 1-week period in February to smoothly connect with the previous year's fields. In these initial simulations, tests for long-term family and species conservation were of interest and the use of a single year of repeating flow fields effectively removes uncertainties which arise from model-calculated interannual variability.

The model was initialized with zonal mean conditions for each of the 15 families and species. These initial profiles were either bootstrapped from previous model runs or taken from a two-dimensional model simulation [Garcia and Solomon, 1982]. Within 3 years the model reached a cyclical steady state condition with excellent repeatability in subsequent years.

A parameterized scheme to represent the impact of polar stratospheric cloud (PSC) chemistry is enabled in some of our model integrations. A previous effort to incorporate heterogeneous chemistry into the model was described by Eckman *et al.* [1993], but the current scheme has a better representation of these processes. Four heterogeneous reactions (reactions (68), (73), (76), and (80) in Table 3) considered important in the repartitioning of the nitrogen and chlorine families are included. In the case of the reactions involving $\text{H}_2\text{O}(\text{s})$, a first-order rate constant of $4.0 \times 10^{-6} \text{ s}^{-1}$ is used. Those reactions involving $\text{HCl}(\text{s})$ employ a second-order reaction rate of $1.5 \times 10^{-14} \text{ cm}^3 \text{ s}^{-1}$. The reaction of HOCl with HCl on PSCs is not included in the current scheme. Prather [1992] showed that this reaction provides an additional mechanism for chlorine activation in Antarctic springtime that improves the agreement of models with observations. Our results therefore probably underestimate polar ozone destruction.

These heterogeneous processes occur when the GCM-calculated temperature is less than 195 K and is limited to pressures greater than 20 mbar. The NAT formation criterion is, in this instance, decoupled from the HNO_3 distribution. This reduces the level of realism in the simulation; however, a highly detailed scheme was deemed to be of little additional benefit as the GCM-calculated temperatures reflect a cold pole bias, particularly in the southern hemisphere [e.g., Mahlman and Umscheid, 1984] and extend too high in the southern polar stratosphere to employ a detailed PSC formation scheme. Our intention, rather, is

to provide a mechanism for allowing polar processing to occur in the model and to analyze its first-order effects in a three-dimensional formulation.

A weak removal of odd nitrogen from the system with a 30-day time constant occurs whenever this temperature threshold is reached, similar to a scheme employed by Granier and Brasseur [1992]. When the temperature is less than 186K, stronger denitrification takes place with a time constant of 5 days. While we make no distinction between type I and type II PSCs in the NAT tracer, the stronger sedimentation implied by the faster denitrification at and below approximate type II formation temperatures takes account of the larger size and faster fall rate of type II PSCs [e.g., Turco *et al.*, 1989]. Evaporation of the NAT occurs when temperatures rise above 195 K, with a time constant of 1 day. Dehydration, known to occur in the stratosphere during Antarctic springtime as a result of the sedimentation of cloud particles [e.g., Kelly *et al.*, 1989], is not currently accounted for in the model as H_2O is not explicitly calculated.

The role of sulfate aerosols on stratospheric chemistry has been unambiguously demonstrated [e.g., Rodriguez *et al.*, 1991; Fahey *et al.*, 1993]. One model simulation includes a parameterization of chemistry occurring on stratospheric sulfate aerosols using the recommendations made in WMO [1991] which yield first-order loss rates for N_2O_5 and ClONO_2 on water in aerosol. We use sulfate aerosol values that are 2 times the minimum levels given in WMO [1991], consistent with values used by Garcia and Solomon [1994] which are representative of levels observed during the late 1980s. As comparisons are made with UARS measurements following the eruption of Mount Pinatubo in June 1991, an additional short run was performed to investigate model sensitivity with aerosol levels 8 times the minimum values in WMO [1991]. This aerosol distribution has surface areas of approximately $10 \mu\text{m}^2 \text{ cm}^{-3}$ in the lower stratosphere which are reasonably consistent with those used by Tie *et al.* [1994] to simulate the mid-1992 period.

Model Morphology

A 7-year simulation of the CTM was performed to investigate the stability of various families and species in response to a long time integration. In previous versions of the model the long-term behavior of the odd nitrogen and odd chlorine families revealed that they were not well conserved. The inclusion of explicit transport of N_2O and the chlorine source gases has now solved these difficulties.

We present results from the three-dimensional simulation focusing on total ozone behavior, the zonal mean

species distributions, and species distributions on pressure surfaces to show longitudinal structure. Total ozone is compared with observed climatologies to reveal basic model performance and its ability to simulate this critical constituent. Zonal mean distributions describe the seasonal evolution and the vertical distribution of atmospheric species. Surface distributions show the effects of both diurnal chemistry and dynamical processes in these species.

Total Ozone

Figure 1a shows the total odd oxygen column versus latitude as a function of time for the final year of the 7-year simulation. This simulation employed only gas phase chemistry. Compared with the total ozone mapping spectrometer (TOMS) satellite ozone climatology for the 1980s shown in Figure 1b [Newman, 1993], the agreement is reasonable except in southern high-latitude springtime. A low-latitude minimum is seen with some movement of the minimum levels about the equator in accord with these observations. Tropical levels of 220 Dobson units (DU) are somewhat below the 260 DU minimum seen in these observations. The lack of multiple scattering in our photolysis rate scheme may explain the tropical differences noted. However, the high-latitude northern winter maximum with levels of around 480 DU is in good accord with an average of TOMS observations made during the 1980s. The model calculated a southern hemisphere winter/spring maximum of about 300 DU which is lower than the levels of 360 DU seen in the 1980s TOMS observations and in a pre-1980 ozone climatology based on ground-based observations [London, 1980]. There are only hints of the poleward progression of the maximum in the late southern spring.

A 1-year simulation with parameterized PSC and sulfate aerosol chemistry was also performed. Initial conditions were taken from the gas phase model in June of model year 6 and run forward for 1 year. The gas phase results for the final model year can therefore be considered a baseline for comparison with this heterogeneous chemistry run.

Figure 2, to be compared with Figure 1a, shows the corresponding total ozone versus latitude plot for the 1-year simulation which includes both PSC and sulfate aerosol chemistry. During southern springtime a substantial high-latitude ozone depletion is seen, with levels of total ozone reduced to approximately 180 DU during October, about 35% below the values seen in the gas phase run. This is somewhat higher than the levels measured by the TOMS instrument during most years of the 1980s and, to some extent, reflects the difference between heterogeneous chem-

istry temperature thresholds based on the GCM-calculated temperatures and those in the real atmosphere for a given year. The lack of bromine chemistry, responsible for about 25% of the observed springtime southern hemispheric ozone depletion, also accounts for part of this difference [e.g., WMO, 1991]. Little difference is seen in column ozone levels in the northern hemisphere winter or spring between the heterogeneous chemistry run and the control simulation.

The calculated springtime ozone depletion is longer-lived compared with TOMS observations which show recovery during October during the 1980s. The transition from winter to spring in the model simulation of the southern hemisphere is more radiatively controlled and slower than in the true atmosphere, as revealed by the time series of calculated temperatures at 45 mbar shown in Figure 3. Here, temperatures poleward of 60°S remain below 195 K until mid-November. For this reason, recovery of our model ozone hole is delayed until the November/December time period.

Zonal Mean Distributions

The seasonal variation of several key model constituents is presented in Figures 4 through 8 and compared, where available, with measurements made by instruments aboard the UARS satellite. Midmonth zonal mean mixing ratios are presented for January and June from the simulation that included both PSC and sulfate aerosol chemistry. The selection of the January UARS data was dictated by the choice of January 9–11, 1992, by the UARS science team as a special period for intensive validation studies (J. C. Gille and W. L. Grose, Upper Atmosphere Research Satellite Validation Workshop III Report: Temperature and Constituents, September 20–24, 1993, unpublished manuscript (hereinafter GG94)). In addition, the UARS spacecraft yawed in mid-January to a southward viewing orientation. It should be emphasized that the conditions simulated in a free-running GCM simulation are not expected to reproduce the precise conditions for a given day of UARS observations. Here instead, we use these zonal mean observations to elucidate general model processes and behavior.

Figure 4 shows the modeled ozone mixing ratio compared with observations made by the microwave limb sounder (MLS) using 205-GHz radiometer, version 3/3AL data [Barath *et al.*, 1993] as a function of latitude and pressure. Maximum values of approximately 11 parts per million by volume (ppmv) in the equatorial midstratosphere are observed and are well reproduced by the model. The location of the peak mixing ratio traverses the equator, following

the subsolar point, in agreement with MLS measurements. This feature is also similar to the long-term behavior observed by the solar backscatter ultraviolet (SBUV) experiment aboard Nimbus 7 [e.g., *Perliski and London*, 1989].

The model exhibits some lifting of the mixing ratio isopleths in altitude toward high latitudes in winter, particularly in the southern hemisphere in June. This behavior is very pronounced in the June MLS measurements. *Perliski and London* [1989] assert that this upward tilt toward the winter hemisphere in the upper stratosphere results from both the temperature-dependent photochemistry and the effective upward ozone transport at subpolar latitudes in winter. We ran a 1-month simulation with chemistry disabled and initialized with the odd oxygen field on June 1 in an attempt to isolate the dynamical effects. The model odd oxygen field rapidly lost its upward tilt toward the winter hemisphere. Thus the temperature-dependent photochemistry is the driving process for the upper stratospheric tilt in our model. The effect is much less pronounced in both model and observation in the northern hemisphere winter. This is consistent with the warmer middle- and high-latitude northern hemispheric wintertime temperatures calculated by the GCM as shown in Figure 5 and, less strikingly, in the real atmosphere.

Calculated upper stratospheric ozone underestimates observation by approximately 10–20%, which remains a common feature in many stratospheric models [e.g., *McPeters*, 1993]. Although MLS data may be slightly high (for example, there is an observed 5–10% bias in MLS versus stratospheric aerosol and gas experiment II ozone data (D. Cunnold, private communication, 1992)), it is believed that most of the discrepancy is not caused by the observations.

Zonally averaged HNO_3 from the cryogenic array etalon spectrometer (CLAES) instrument [*Roche et al.*, 1993] using version 7/3AL data together with the model calculation are presented in Figure 6. As with observations, the model distribution reveals most HNO_3 residing away from the tropics, peaking near the poles. Maxima are observed in southern and northern high latitudes with a peak value in excess of 10 parts per billion by volume (ppbv) in the southern hemisphere in June, compared with a model value of 12 ppbv. The January northern hemispheric peak of 12 ppbv compares with a value of 10 ppbv calculated by the model. As HNO_3 measurement accuracy is estimated to be in the 20% range in the lower stratosphere [*Roche et al.*, 1994], these differences between model and measurement may not be significant. The maxima are observed at slightly lower altitudes than our model calculations predict.

A simulation with higher aerosol surface areas rep-

resentative of the conditions following the eruption of Mount Pinatubo yielded HNO_3 values approximately 1 ppbv larger throughout the midstratosphere compared with the baseline aerosol case shown in Figure 6. These results (not shown) are in slightly better agreement with the CLAES measurements.

A substantial model seasonal asymmetry is apparent, in fair agreement with earlier observations made by the Nimbus 7 limb infrared monitor of the stratosphere (LIMS) experiment [*Russell*, 1986] although the high-latitude southern winter values seem too high compared with observation. The results are dramatically improved with respect to the model simulation which did not include the effects of sulfate aerosol chemistry (not shown). In that simulation, high-latitude wintertime HNO_3 was approximately a factor of 2 less abundant at the maximum, consistent with early studies by *Austin et al.* [1986].

The sharp gradient in HNO_3 in the June CLAES observations near 80°S does not appear in the model calculations. *Roche et al.* [1994] ascribe this depleted region of HNO_3 to removal through NAT formation. In the model simulation, conversion of HNO_3 to condensed forms at these high southern latitudes has proceeded for a relatively short time and a distinct collar region surrounding the vortex does not become apparent until the following month. This is because the heterogeneous calculations were initiated on June 1 using species values from the gas phase simulation.

Model calculations of ClONO_2 in January and June are compared with 1992 CLAES observations in Figure 7 using version 7/3AL data. The January northern high-latitude peak of 1.2 ppbv is in reasonable accord with observation. The height of the middle- and low-latitude model peak occurs slightly higher than observation, at 15 mbar. The agreement at high latitudes in January is much improved in this instance because of the inclusion of sulfate chemistry. A simulation with only PSC heterogeneous processes yielded values of ClONO_2 of the order of 1.6 ppbv (not shown). However, CLAES ClONO_2 measurement accuracies are estimated at 30% in the lower stratosphere [*Roche et al.*, 1994], so that it remains somewhat ambiguous how the inclusion of sulfate aerosol processes affects model/measurement agreement in this instance.

In contrast, the calculated loss of ClONO_2 due to reaction on sulfate aerosols in southern high latitudes in June yields levels much lower than observation. Although there is some evidence of a highly depleted region of ClONO_2 in CLAES observations poleward of 80°S in the lower stratosphere in rough accord with the model, the observed peak at 65°S at 15 mbar is wholly absent from the model. The cause of this model-calculated high-latitude depleted

region below the 20-mbar level is due to the sulfate aerosol processing, magnified by the model cold pole bias which accelerates this temperature-dependent process. The simulation with higher sulfate aerosol loading representative of the mid-1992 period (not shown) reveals that the highly depleted region of ClONO_2 extends both higher and more equatorward than in the baseline aerosol case. These results suggest that differences in the specified geographical distribution of sulfate aerosol in the model compared with its distribution in the real atmosphere may account for this discrepancy.

The distributions of two longer-lived constituents, total odd nitrogen and total odd chlorine, are shown in Figure 8 for mid-January and mid-June. In the case of NO_y , shown in the top two panels of the figure, a maximum value of 22 ppbv at the 3-mbar level is seen. The altitude of the peak decreases toward the poles in agreement with the NO_y distributions inferred from summing nighttime NO_2 and HNO_3 from observations made by LIMS [Callis *et al.*, 1985]. However, the peak NO_y level from the model is higher than the 16–17 ppbv levels inferred from measurements made by the atmospheric trace molecule spectroscopy (ATMOS) experiment in May 1985 [Russell *et al.*, 1988]. Recent revisions of the line parameters used in the LIMS retrievals now yield lower NO_2 levels. LIMS nighttime NO_2 retrieved with this new algorithm agree favorably with measurements of sunset NO_2 plus NO made by the halogen occultation experiment (HALOE) aboard UARS in the upper stratosphere [Remsberg *et al.*, 1994]. Hence the inferred peak NO_y levels of 22.5 ppbv from the work of Callis *et al.* [1985] may be too high. Nonetheless, these model NO_y results are much improved compared with earlier formulations of the chemistry-transport module before we explicitly transported the source gas N_2O .

Analysis of the correlations of long-lived stratospheric species has provided insight into chemical and dynamical processes [e.g., Plumb and Ko, 1992]. It has been shown that under some circumstances these correlation relationships may yield useful proxies for the determination of an unobserved constituent or as evidence for the occurrence of processes such as denitrification in the high-latitude winter stratosphere [Fahey *et al.*, 1990].

The correlation of our calculated NO_y and N_2O is shown in Plate 1. In Plate 1 (left) the correlations at all model grid points between the 400 K and the 850 K isentropic surfaces, approximately from 70 mbar to 10 mbar, utilizing the PSC/sulfate aerosol simulation are displayed. The correlations are further separated as a function of latitude. Several regimes are seen. Throughout the lower stratosphere where N_2O abundance is above approximately 100 ppbv, a region of negative correlation is

seen. This region is relatively compact, i.e., with little scatter at N_2O levels above 200 ppbv. Correlations in the tropical region show increased scatter at N_2O levels above 200 ppbv which lie higher in the stratosphere in the region of chemical production of NO_y . A much more diffuse area of correlation with curvature is seen at levels of N_2O below 100 ppbv in the upper stratosphere. Plumb and Ko [1992] show that the curvature in the correlation is a manifestation of the shorter chemical lifetime of NO_y in the upper stratosphere.

We isolate the lower stratospheric region of compact, linear correlation in Plate 1 (right). Here, the model results are restricted to levels between 400 K and 500 K. A least squares fit to the data yields a slope of -0.08, somewhat higher than the -0.07 slope deduced by Fahey *et al.* [1990] from airborne measurements in the Arctic and in reasonable accord with the model-derived slope of -0.074 from the analysis of Plumb and Ko [1992] who also reason that such correlation studies should be applicable to three-dimensional data. Our model results support the assertion that their conceptual framework applies in the three-dimensional sense.

Total odd chlorine, Cl_y , is displayed on the bottom panel of Figure 8 for the two time periods considered above. As expected from photochemical theory, a rapid increase with height in Cl_y is revealed in the lower stratosphere where photolysis of the chlorine source gases is most efficient. The maximum Cl_y level is calculated to occur in a broad region in the middle and upper stratosphere. Relatively little variation with season is seen, although the bulge with altitude near the equator shows signs of following the subsolar point. The maximum level of Cl_y in the upper stratosphere is 3.30 ppbv compared with a summed total surface chlorine source of 3.32 ppbv, indicating that the 7-year model spin-up period was adequate.

Odd Chlorine Family

We examine the distribution of members of the odd chlorine family to characterize model performance and attempt to constrain model behavior to available measurements. We focus on the period during southern hemisphere springtime where observations of enhanced active chlorine are made by UARS instruments. We also study the impact of the inclusion of the channel to HCl from the reaction of $\text{ClO} + \text{OH}$.

Antarctic Springtime

A useful perspective is provided by examining the results of the model on a global projection at a given pressure or potential temperature surface. Evidence of longi-

tudinal asymmetries and diurnal chemical effects may be obtained. However, there are relatively few global data sets to compare directly in this manner. An orthographic projection was selected, centered somewhat arbitrarily at 60°S and 105°W , so that low-latitude behavior is also represented. We use the results of the model which include both polar heterogeneous and sulfate aerosol processes unless otherwise specified.

The location of the model-calculated southern polar vortex on September 14 is identified by the potential vorticity map at 450 K shown in Figure 9. We normalize the potential vorticity by dividing by its maximum. A region of high potential vorticity with sharp gradient poleward of 60°S defines the approximate location of the vortex which is offset from the pole toward the Palmer peninsula.

Figure 10 shows the calculated temperature at 45 mbar for September 14. The region of temperatures below the specified NAT threshold of 195 K is clearly evident, extending poleward of approximately 60°S . Minimum temperatures lie near the vortex center shown in Figure 9. A corresponding region of enhanced NAT is apparent in Figure 11 with some of the NAT extended slightly north of the temperature threshold boundary, probably due to the inability of the relatively low horizontal resolution of the present model to maintain very sharp gradients. A broad area of very low NAT within the vortex is calculated between 25°W and 185°W , corresponding to temperatures below the 186K threshold for enhanced sedimentation. Levels of NAT are low throughout the vortex area at this time owing to the denitrification that has been occurring since July.

Corresponding to the occurrence of NAT, a region of enhanced lower stratospheric ClO is evident in Figure 12. The sharp gradient at 105°W is due to the location of the terminator for this particular snapshot in time. West of that longitude, the Antarctic continent is in darkness and active chlorine is in forms other than ClO, such as Cl_2O_2 shown in Figure 13. Cl_2O_2 is present throughout the region of low temperatures but is much enhanced in darkness, as expected from photochemical theory.

Figure 14 shows the model ClONO_2 field for the same period. Essentially all ClONO_2 is removed from the vortex region with a region of enhancement in a collar surrounding the vortex, in good agreement with CLAES observations [see Roche *et al.*, 1994, Figure 8a] which show little ClONO_2 poleward of the collar surrounding the vortex in springtime. With no sulfate aerosol processes, our model predicts appreciable levels of ClONO_2 within the vortex region on this date, as shown in Figure 15. While it is tempting to attribute the improved agreement between model and measurement to the addition of the ClONO_2 re-

action with water on sulfate aerosols, the lack of detailed aerosol microphysics in the chemistry code does not enable us to make this conclusion unambiguously.

Chlorine Partitioning

Using MLS ClO and HALOE HCl measurements, we examine the impact of the inclusion of the additional pathway to HCl from the $\text{ClO} + \text{OH}$ reaction, as suggested by Toumi and Bekki [1993] and Natarajan and Callis [1991]. Simulations were run both with and without reaction (81) (see Table 3). In the following discussion we define “standard chemistry” as the simulation without the additional pathway to HCl enabled but with PSC and sulfate chemistry included.

Measurements of HCl from HALOE are shown in Figure 16a taken on September 13, 1992, and plotted as a daytime average versus pressure using version 16/level 2 data [Russell *et al.*, 1993]. HALOE-viewing geometry yields measurements in a localized latitude range on a given day. We chose to average the daytime data given the difficulty of finding coincident measurements made by other instruments at the same local time. Single profile HCl measurement accuracies are estimated to be 16% at 1 mbar, 11% at 3 mbar, and 13% at 10 mbar (J. M. Russell III, private communication, 1994). Also shown are the corresponding daytime-averaged model profiles using standard chemistry and with the additional HCl pathway included (denoted “ $\text{ClO} + \text{OH}$ ”). In this instance, agreement between measurement and model is improved with the inclusion of the $\text{ClO} + \text{OH}$ reaction at pressures below the 1-mbar level.

Daytime-averaged MLS ClO measurements using version 3/3AL data for the corresponding latitude of 35.4°S are presented in Figure 16b. The use of daytime-averaged data reduces measurement noise (GG94) and yields a consistent comparison with the HCl data. Analogous to the situation with HCl, the inclusion of the additional pathway lessens the calculated abundance of ClO, and the agreement between measurement and model is improved in the upper stratosphere compared to the standard chemistry case. Examination of results from adjacent days and adjacent latitudes shows this to be a robust result. In all instances the agreement between MLS-measured ClO and the model at middle latitudes in the southern hemisphere is improved by including the additional HCl pathway.

At higher southern latitudes the situation remains broadly similar. Figures 16c and 16d show corresponding HCl and ClO plots for September 20, 1992, at 55.2°S . Coincident measurements at higher latitudes are not available during this period as the spacecraft’s yaw maneuver occurred on the following day. HALOE HCl continues to be modeled better with the inclusion of the additional reac-

tion although absolute agreement, particularly in the lower stratosphere, is less good than the midlatitude case. The MLS ClO measurements also show better agreement with the inclusion of the additional reaction pathway.

Some disagreement has been noted between MLS ClO measurements in the springtime polar upper stratosphere and ground-based microwave measurements during the austral spring of 1987 made by *deZafra et al.* [1989]. The ground-based measurements revealed levels of upper stratospheric ClO as high as 1.6 ppbv, compared with MLS-measured levels of approximately 1.0 ppbv at high latitudes. These high levels are not supported by the model results noted above when the additional reaction channel is enabled.

While these results are encouraging, several uncertainties remain. Comparisons of the model-specified CH₄ mixing ratio and HALOE measurements reveal some differences, with the model CH₄ values falling slightly below HALOE measurements in the upper stratosphere. Enhanced CH₄ at these levels would tend to reduce active chlorine further. It would also be useful to have measurements of OH to further pursue studies of odd chlorine partitioning.

Also evident in the ClO comparison in Figure 16d is a region of enhanced active chlorine in the lower stratosphere around 30 mbar in the model results. This enhanced region of active chlorine from PSC processing extends to somewhat lower latitudes than those revealed by the spatial extent of enhanced ClO from MLS. The tendency for modeled HCl to underestimate HALOE measurements below 25 mbar (as shown in Figure 16c) is due to the change in partitioning in favor of active chlorine.

Concluding Remarks

The results of a long-term simulation of stratospheric chemical species have been presented. Additional runs incorporating parameterized polar heterogeneous processes and reactions on sulfate aerosol particles were also performed.

The agreement between model calculations of the seasonal and latitudinal variation of total ozone are reasonable, albeit with differences in detail. For example, our simulated southern polar ozone depletion is less deep and somewhat longer-lived than satellite observations during the 1980s, due possibly to the lack of bromine chemistry and the differences between the observed and the modeled dynamical evolution of the southern polar vortex.

Comparisons of model zonal mean distributions with UARS measurements were made during two time periods in January, during a period of intensive UARS constituent

and temperature validations, and in June to provide insight into seasonal variability. It should be emphasized that these simulations do not represent the thermal and dynamical conditions on a particular date. Therefore conclusions derived from comparisons of data for particular time periods with a free-running GCM must necessarily be somewhat limited.

Agreement with MLS ozone observations is good. The lifting of the mixing ratio isopleths toward high latitudes in winter is reproduced in the southern hemisphere and is a consequence of the model photochemistry. The equatorial ozone maximum is reproduced well although the model exhibits a deficit with respect to measurements in the upper stratosphere, in common with most theoretical models.

Comparisons with CLAES HNO₃ observations reveal satisfactory agreement at high latitudes only when sulfate aerosol chemistry is included. The CLAES ClONO₂ observations reveal differences with theory, particularly at southern high latitudes. Our model results suggest a “competition” between PSC and sulfate aerosol processes. Box models including the detailed microphysics of both PSC and sulfate processes may assist in identifying these discrepancies.

An examination of the correlation of model calculations of N₂O with NO_y supports the utility of this method in a three-dimensional framework. The calculated effective conversion efficiency between N₂O and NO_y is slightly larger than a value derived from polar aircraft measurements [*Fahey et al.*, 1990].

Modeled distributions of members of the odd chlorine family in the lower stratosphere during austral springtime reveal enhanced active chlorine as a result of polar processing, both by PSCs and sulfate aerosols. Levels of ClO at 45 mbar are enhanced from near zero (with gas phase chemistry) to 1.4 ppbv with the PSC/sulfate chemistry enabled in the cold vortex where NAT formation occurs. The diurnal variation of active chlorine is evident in the model with nighttime repartitioning into other forms, such as HOCl and Cl₂O₂. The observed relationship of UARS ClO and HCl in the upper stratosphere is modeled better by the inclusion of an additional pathway yielding HCl from the ClO + OH reaction, as suggested by *Natarajan and Callis* [1991] and *Toumi and Bekki* [1993].

Overall, the performance of the CTM is satisfactory in many key respects. Its ability to simulate the seasonal evolution of ozone and other key stratospheric constituents lends confidence to the chemical and dynamical approaches employed. As noted above, some shortcomings can be explained by the model’s modest horizontal resolution and lack of detail in some areas of its chemical scheme.

Several model improvements are currently being implemented to address these issues. The horizontal resolution of both the GCM and the CTM is in the process of being increased from T16 to T32. Initial results from these simulations look promising with evidence of an improved calculated thermal structure. These new versions of the GCM and CTM will be coupled to allow for explicit feedback between the calculated ozone and the radiative calculation in the GCM. We plan to summarize the findings of these simulations in the near future.

Planned improvements to the chemistry module include the addition of bromine chemistry, necessary for a more quantitative examination of lower-stratospheric polar processes. The photolysis calculation routine will be improved with a characterization of multiple scattering. We will explicitly transport the remaining long-lived species, specifically CH₄ and H₂O, to provide for enhanced model realism and improve its utility for making comparisons with available measurements. In addition, a more realistic treatment of heterogeneous processes associated with background sulfate aerosols will be incorporated into the CTM following the formulation of *Hanson et al.* [1994] to examine its potential global impact on ozone and other trace stratospheric constituents.

Acknowledgments. This model was developed under the auspices of the NASA UARS program. We are grateful to Ellis Remsberg and David Siskind for suggesting improvements to an earlier version of this manuscript.

References

- Austin, J., R. R. Garcia, J. M. Russell III, S. Solomon, and A. F. Tuck, On the atmospheric photochemistry of nitric acid, *J. Geophys. Res.*, *91*, 5477–5485, 1986.
- Barath, F. T., et al., The Upper Atmosphere Research Satellite microwave limb sounder instrument, *J. Geophys. Res.*, *98*, 10,751–10,762, 1993.
- Baulch, D. L., R. A. Cox, P. J. Crutzen, R. F. Hampson Jr., J. A. Kerr, J. Troe, and R. T. Watson, Evaluated kinetic and photochemical data for atmospheric chemistry, Supplement 1, CO-DATA task group on chemical kinetics, *J. Phys. Chem. Ref. Data*, *11*, 327–496, 1982.
- Blackshear, W. T., W. L. Grose, and R. E. Turner, Simulated sudden stratospheric warming, Synoptic evolution, *Q. J. R. Meteorol. Soc.*, *113*, 815–846, 1987.
- Callis, L. B., M. Natarajan, and J. M. Russell III, Estimates of the stratospheric distribution of odd nitrogen from the LIMS data, *Geophys. Res. Lett.*, *12*, 259–262, 1985.
- Chipperfield, M. P., D. Cariolle, and P. Simon, A three-dimensional modeling study of trace species in the Arctic lower stratosphere during winter 1989–1990, *J. Geophys. Res.*, *98*, 7199–7218, 1993.
- DeMore, W. B., et al., Chemical kinetics and photochemical data for use in stratospheric modeling, in Evaluation 9, *JPL Publ. 90-1*, Jet Propul. Lab., Pasadena, Calif., 1990.
- deZafra, R. L., M. Jaramillo, L. K. Emmons, P. M. Solomon, and A. Parrish, New observations of a large concentration of ClO in the springtime lower stratosphere over Antarctica and its implications for ozone-depleting chemistry, *J. Geophys. Res.*, *94*, 11,423–11,428, 1989.
- Eckman, R. S., R. E. Turner, W. T. Blackshear, T. D. A. Fairlie, and W. L. Grose, Some aspects of the interaction between chemical and dynamical processes relating to the Antarctic ozone hole, *Adv. Space Res.*, *13*, 311–319, 1993.
- Fahey, D. W., S. Solomon, S. R. Kawa, M. Loewenstein, J. R. Podolske, S. E. Strahan, and K. R. Chan, A diagnostic for denitrification in the winter polar stratospheres, *Nature*, *345*, 698–702, 1990.
- Fahey, D. W., et al., In situ measurements constraining the role of sulphate aerosols in mid-latitude ozone depletion, *Nature*, *363*, 509–514, 1993.
- Frederick, J. E., et al., Radiative processes: Solar and terrestrial, in *Atmospheric Ozone 1985*, pp. 349–392, *WMO Rep. 16*, World Meteorol. Organ., Geneva, 1986.
- Garcia, R. R. and S. Solomon, A numerical model of the zonally averaged dynamical and chemical structure of the middle atmosphere, *J. Geophys. Res.*, *87*, 1379–1400, 1982.
- Garcia, R. R. and S. Solomon, A new numerical model of the middle atmosphere, 2, Ozone and related species, *J. Geophys. Res.*, *99*, 12,937–12,951, 1994.
- Gidel, L. T., P. J. Crutzen, and J. Fishman, A two-dimensional photochemical model of the atmosphere, 1, Chlorocarbon emissions and their effect on stratospheric ozone, *J. Geophys. Res.*, *88*, 6622–6640, 1983.
- Granier, C., and G. Brasseur, Impact of heterogeneous chemistry on model predictions of ozone changes, *J. Geophys. Res.*, *97*,

- 18,015–18,033, 1992.
- Grose, W. L., J. E. Nealy, R. E. Turner, and W. T. Blackshear, Modeling the transport of chemically active constituents in the stratosphere, in *Transport Processes in the Middle Atmosphere*, pp. 229–250, edited by G. Visconti and R. Garcia, D. Reidel, Norwell, Mass., 1987.
- Grose, W. L., R. S. Eckman, R. E. Turner, and W. T. Blackshear, Antarctic ozone depletion and potential effects on the global ozone budget, in *Dynamics, Chemistry and Photochemistry in the Middle Atmosphere of the Southern Hemisphere*, edited by A. O'Neill and C. R. Mechoso, Kluwer Acad., Norwell, Mass., 1990.
- Hanson, D. R., A. R. Ravishankara, and S. Solomon, Heterogeneous reactions in sulfuric acid aerosols: A framework for model calculations, *J. Geophys. Res.*, *99*, 3615–3629, 1994.
- Hoskins, B. J., and A. J. Simmons, A multi-layer model and the semi-implicit method, *Q. J. R. Meteorol. Soc.*, *101*, 637–655, 1975.
- Kaye, J. A., and R. B. Rood, Chemistry and transport in a three-dimensional stratospheric model: Chlorine species during a simulated stratospheric warming, *J. Geophys. Res.*, *94*, 1057–1083, 1989.
- Kelly, K. K., et al., Dehydration in the lower Antarctic stratosphere during late winter and early spring, 1987, *J. Geophys. Res.*, *94*, 11,317–11,357, 1989.
- Lary, D. J., J. A. Pyle, and G. Carver, A three-dimensional model study of nitrogen oxides in the stratosphere, *Q. J. R. Meteorol. Soc.*, *120*, 453–482, 1994.
- Lefèvre, F., G. P. Brasseur, I. Folkins, A. K. Smith, and P. Simon, Chemistry of the 1991–1992 stratospheric winter: Three-dimensional model simulations, *J. Geophys. Res.*, *99*, 8183–8195, 1994.
- London, J., The observed distribution and variations of total ozone, in *Proceedings of the NATO Advanced Studies Institute on Atmospheric Ozone*, pp. 31–44, edited by M. Nicolet and A. Aikin, U.S. Dep. of Transp., Washington, D.C., 1980.
- London, J., and J. H. Park, The interaction of ozone photochemistry and dynamics in the stratosphere, A three-dimensional atmospheric model, *Can. J. Chem.*, *52*, 1599–1609, 1974.
- Mahlman, J. D., and L. J. Umscheid, Dynamics of the middle atmosphere: Successes and problems of the GFDL “Skyhi” general circulation model, in *Dynamics of the Middle Atmosphere*, pp. 501–525, edited by J. R. Holton and T. Matsuno, Terra Sci., Tokyo, 1984.
- McElroy, M. B., and R. J. Salawitch, Changing composition of the global stratosphere, *Science*, *243*, 763–770, 1989.
- McPeters, R., Ozone profile comparisons, in *The Atmospheric Effects of Stratospheric Aircraft: Report of the 1992 Models and Measurements Workshop*, pp. D1–D37, edited by M. J. Prather and E. E. Remsberg, *NASA Ref. Publ. 1292*, Washington, D.C., 1993.
- Natarajan, M., and L. B. Callis, Stratospheric photochemical studies with Atmospheric Trace Molecule Spectroscopy (ATMOS) measurements, *J. Geophys. Res.*, *96*, 9361–9370, 1991.
- Newman, P. A., Comparison of modeled and measured total column ozone, in *The Atmospheric Effects of Stratospheric Aircraft: Report of the 1992 Models and Measurements Workshop*, pp. C1–C22, edited by M. J. Prather and E. E. Remsberg, *NASA Ref. Publ. 1292*, 1993.
- Perliski, L. M., and J. London, Satellite-observed long-term averaged seasonal and spatial ozone variations in the stratosphere, *Planet. Space Sci.*, *37*, 1509–1525, 1989.
- Phillips, N. A., A coordinate system having some special advantages for numerical forecasting, *J. Meteorol.*, *14*, 184–185, 1957.
- Pierce, R. B., W. T. Blackshear, T. D. Fairlie, W. L. Grose, and R. E. Turner, The interaction of radiative and dynamical processes during a simulated sudden stratospheric warming, *J. Atmos. Sci.*, *50*, 3829–3851, 1993.
- Plumb, R. A., and M. K. W. Ko, Interrelationships between mixing ratios of long-lived stratospheric constituents, *J. Geophys. Res.*, *97*, 10,145–10,156, 1992.
- Prather, M. J., More rapid polar ozone depletion through the reaction of HOCl with HCl on polar stratospheric clouds, *Nature*, *355*, 534–537, 1992.
- Remsberg, E. E., P. R. Bhatt, R. S. Eckman, L. L. Gordley, J. M. Russell, III, and D. E. Siskind, Effect of the Hitran 92 spectral data on the retrieval of NO₂ mixing ratios from Nimbus 7 LIMS, *J. Geophys. Res.*, *99*, 22,965–22,973, 1994.
- Roche, A. E., et al., The cryogenic array etalon spectrometer (CLAES) on UARS: Experiment description and performance, *J. Geophys. Res.*, *98*, 10,763–10,775, 1993.
- Roche, A. E., J. B. Kumer, J. L. Mergenthaler, R. W. Nightingale, W. G. Uplinger, G. A. Ely, J. F. Potter, D. J. Wuebbles, P. S. Connell, and D. E. Kinnison, Observations of lower-stratospheric ClONO₂, HNO₃, and aerosol by the UARS CLAES experiment between January 1992 and April 1993, *J. Atmos. Sci.*, *51*, 2877–2902, 1994.
- Rodriguez, J. M., M. K. W. Ko, and N. D. Sze, Role of heterogeneous conversion of N₂O₅ on sulphate aerosols in global ozone losses, *Nature*, *352*, 134–137, 1991.
- Russell, J. M., III (Ed.), *Handbook for MAP*, vol. 22, 302 pp., Int. Counc. of Sci. Unions, Sci. Comm. on Solar-Terr. Phys., Urbana, Ill., 1986.
- Russell, J. M., III, C. B. Farmer, C. P. Rinsland, R. Zander, L. Froidevaux, G. C. Toon, B. Gao, J. Shaw, and M. Gunson, Measurements of odd nitrogen compounds in the stratosphere by the ATMOS experiment on Spacelab 3, *J. Geophys. Res.*, *93*, 1718–1736, 1988.
- Russell, J. M., III et al., The Halogen Occultation Experiment, *J. Geophys. Res.*, *98*, 10,777–10,797, 1993.
- Smith, F. L., III, and C. Smith, Numerical evaluation of Chapman's grazing incidence integral ch(X,χ), *J. Geophys. Res.*, *77*, 3592–3597, 1972.
- Stolarski, R. S., and H. L. Wesoky (Eds.), *The atmospheric effects of stratospheric aircraft: A third program report*, *NASA Ref. Publ. 1313*, 1993.
- Tie, X., G. P. Brasseur, B. Briegleb, and C. Granier, Two-dimensional simulation of Pinatubo aerosol and its effect on stratospheric ozone, *J. Geophys. Res.*, *99*, 20,545–20,562, 1994.
- Toumi, R., and S. Bekki, The importance of the reactions be-

tween OH and ClO for stratospheric ozone, *Geophys. Res. Lett.*, *20*, 2447–2450, 1993.

Turco, R. P., O. B. Toon, and P. Hamill, Heterogeneous physicochemistry of the polar ozone hole, *J. Geophys. Res.*, *94*, 16,493–16,510, 1989.

World Meteorological Organization (WMO), Report of the International Ozone Trends Panel 1988, *WMO Rep. 18*, World Meteorol. Organ., Geneva, 1988.

World Meteorological Organization (WMO), Scientific assessment of ozone depletion: 1991, *WMO Rep. 25*, World Meteorol. Organ., Geneva, 1991.

W. T. Blackshear, R. S. Eckman (corresponding author), W. L. Grose, J. M. Russell III, and R. E. Turner, NASA Langley Research Center, Mail Stop 401B, Hampton, VA 23681-0001 (e-mail: r.s.eckman@larc.nasa.gov)

L. Froidevaux and J. W. Waters, Jet Propulsion Laboratory, 4800 Oak Grove Dr., Pasadena, CA 91109

J. B. Kumer and A. E. Roche, Lockheed Palo Alto Research Laboratory, 3251 Hanover St., Palo Alto, CA 94304.

October 11, 1994; revised March 9, 1995; accepted April 1, 1995.

Figure 1. Total ozone (a) for the final year of the gas phase simulation as a function of latitude versus time and (b) averaged from total ozone mapping spectrometer observations from 1981 to 1989.

Figure 2. Total ozone for the 1-year polar stratospheric cloud (PSC) and sulfate aerosol chemistry simulation as a function of latitude versus time. The initial conditions were taken from the sixth year of the control simulation so that this may be compared with the final year of the gas phase simulation

Figure 3. Time series of calculated zonal mean temperature (K) at 45 mbar as a function of time and latitude.

Figure 4. Zonal mean ozone mixing ratio (parts per million by volume): model calculations using the PSC/sulfate aerosol chemistry simulation for January 13 and June 15 and MLS observations for January 11 and June 15, 1992.

Figure 5. Zonal mean temperature (K): model calculations for January 13 and June 15.

Figure 6. Zonal mean HNO_3 mixing ratio in parts per billion by volume (ppbv): model calculations using the PSC/sulfate aerosol chemistry simulation for January 13 and June 15 and cryogenic array etalon spectrometer (CLAES) observations for January 11 and June 15, 1992.

Figure 7. Zonal mean ClONO_2 mixing ratio (ppbv): Model calculations using the PSC/sulfate aerosol chemistry simulation for January 13 and June 15 and CLAES observations for January 11 and June 15, 1992.

Figure 8. Zonal mean total odd nitrogen (NO_y) and total odd chlorine (Cl_y) mixing ratios (ppbv): Model calculations using the PSC/sulfate aerosol chemistry simulation for January 13 and June 15.

Figure 9. Orthographic projection centered at 60°S and 105°W of general circulation model-calculated normalized potential vorticity on the 450 K isentropic surface for September 14.

Figure 10. Orthographic projection centered at 60°S and 105°W of model temperature on 45-mbar surface for September 14 from PSC/sulfate chemistry simulation.

Figure 11. Same as Figure 10, except for model nitric acid trihydrate mixing ratio (ppbv).

Figure 12. Same as Figure 10, except for model ClO mixing ratio (ppbv).

Figure 13. Same as Figure 10, except for model Cl_2O_2 mixing ratio (ppbv).

Figure 14. Same as Figure 10, except for model ClONO_2 mixing ratio (ppbv).

Figure 15. Same as Figure 14, except for PSC-only simulation (no sulfate chemistry).

Figure 16. (a) Daytime-averaged halogen occultation experiment HCl versus pressure for September 13, 1992, at 35.4°S compared with the daytime-averaged model using standard chemistry and with the inclusion of the $\text{ClO} + \text{OH} \rightarrow \text{HCl} + \text{O}_2$ reaction. (b) As in Figure 16a except for microwave limb sounder ClO . (c) As in Figure 16a except for September 20, 1992, at 55.2°S . (d) As in Figure 16b except for September 20, 1992, at 55.2°S .

Plate 1. (left) Correlation of calculated NO_y with N_2O at all model grid points between 400 K and 850 K isentropic surfaces from the PSC/sulfate aerosol chemistry simulation for January 13. (right) Same as Plate 1 (left) except between 400 K and 500 K surfaces.

Table 1. Chemical Constituents Used in the Model

No.	Constituent
(1)	O ₃
(2)	O
(3)	NO
(4)	NO ₂
(5)	HNO ₃
(6)	HNO ₂
(7)	NO ₃
(8)	H ₂ O ₂
(9)	OH
(10)	HO ₂
(11)	N ₂ O
(12)	N ₂ O ₅
(13)	H ₂ O
(14)	HCl
(15)	CF ₂ Cl ₂
(16)	CFCl ₃
(17)	ClONO ₂
(18)	CH ₄
(19)	CH ₂ O
(20)	CO
(21)	CH ₃ OOH
(22)	CCl ₄
(23)	CH ₃ Cl
(24)	Cl
(25)	ClO
(26)	H
(27)	O(¹ D)
(28)	N
(29)	Cl ₂
(30)	CH ₃
(31)	HCO
(32)	CH ₃ O ₂
(33)	CH ₃ O
(34)	ClO ₂
(35)	O ₂
(36)	H ₂
(37)	CH ₃ CCl ₃
(38)	HOCl
(39)	HO ₂ NO ₂
(40)	Cl ₂ O ₂

Table 2. Photolytic Reactions Used in the Model

No.	Reaction
(1)	$\text{O}_2 + h\nu \rightarrow \text{O} + \text{O}$
(2)	$\text{O}_3 + h\nu \rightarrow \text{O}_2 + \text{O}({}^3\text{P})$
(3)	$\text{O}_3 + h\nu \rightarrow \text{O}_2 + \text{O}({}^1\text{D})$

Table 2. (continued)

No.	Reaction
(4)	$\text{NO}_2 + h\nu \rightarrow \text{NO} + \text{O}$
(5)	$\text{CH}_3\text{CCl}_3 + h\nu \rightarrow 3\text{Cl} + \dots$
(6)	$\text{HNO}_3 + h\nu \rightarrow \text{NO}_2 + \text{OH}$
(7)	$\text{HNO}_2 + h\nu \rightarrow \text{NO} + \text{OH}$
(8)	$\text{H}_2\text{O} + h\nu \rightarrow \text{H} + \text{OH}$
(9)	$\text{H}_2\text{O}_2 + h\nu \rightarrow 2\text{OH}$
(10)	$\text{NO}_3 + h\nu \rightarrow \text{O}_2 + \text{NO}$
(11)	$\text{NO}_3 + h\nu \rightarrow \text{O} + \text{NO}_2$
(12)	$\text{N}_2\text{O} + h\nu \rightarrow \text{N}_2 + \text{O}({}^1\text{D})$
(13)	$\text{N}_2\text{O}_5 + h\nu \rightarrow \text{NO}_2 + \text{NO}_3$
(14)	$\text{NO} + h\nu \rightarrow \text{N} + \text{O}$
(15)	$\text{HCl} + h\nu \rightarrow \text{H} + \text{Cl}$
(16)	$\text{ClO}_2 + h\nu \rightarrow \text{ClO} + \text{O}$
(17)	$\text{ClO} + h\nu \rightarrow \text{Cl} + \text{O}$
(18)	$\text{Cl}_2 + h\nu \rightarrow \text{Cl} + \text{Cl}$
(19)	$\text{CFCl}_3 + h\nu \rightarrow 3\text{Cl} + \dots$
(20)	$\text{CF}_2\text{Cl}_2 + h\nu \rightarrow 2\text{Cl} + \dots$
(21)	$\text{ClONO}_2 + h\nu \rightarrow \text{Cl} + \text{NO}_3$
(22)	$\text{CCl}_4 + h\nu \rightarrow 4\text{Cl} + \dots$
(23)	$\text{CH}_3\text{Cl} + h\nu \rightarrow \text{CH}_3 + \text{Cl}$
(24)	$\text{CH}_2\text{O} + h\nu \rightarrow \text{H} + \text{HCO}$
(25)	$\text{CH}_2\text{O} + h\nu \rightarrow \text{H}_2 + \text{CO}$
(26)	$\text{HOCl} + h\nu \rightarrow \text{Cl} + \text{OH}$
(27)	$\text{HO}_2\text{NO}_2 + h\nu \rightarrow \text{NO}_2 + \text{HO}_2$
(28)	$\text{CH}_3\text{OOH} + h\nu \rightarrow \text{CH}_3\text{O} + \text{OH}$
(29)	$\text{Cl}_2\text{O}_2 + h\nu \rightarrow \text{Cl} + \text{ClO}_2$

Table 3. Chemical Reactions Used in the Model

No.	Reaction	No.	Reaction
(1)	$O_2 + O(^1D) \rightarrow O_2 + O$	(44)	$Cl + O_3 \rightarrow ClO + O_2$
(2)	$N_2 + O(^1D) \rightarrow 2OH$	(45)	$ClO + O \rightarrow Cl + O_2$
(3)	$H_2O + O(^1D) \rightarrow O_3 + M$	(46)	$ClO + NO \rightarrow Cl + NO_2$
(4)	$O + O_2 + M \rightarrow O_3 + M$	(47)	$CH_4 + Cl \rightarrow CH_3 + HCl$
(5)	$O_3 + O \rightarrow 2O_2$	(48)	$H_2 + Cl \rightarrow H + HCl$
(6)	$O + OH \rightarrow H + O_2$	(49)	$Cl + HO_2 \rightarrow HCl + O_2$
(7)	$O + HO_2 \rightarrow OH + O_2$	(50)	$Cl + H_2O_2 \rightarrow HCl + HO_2$
(8)	$NO_2 + O \rightarrow NO + O_2$	(52)	$HOCl + OH \rightarrow ClO + H_2O$
(9)	$Cl + CH_2O \rightarrow HCl + HCO$	(53)	$HCl + OH \rightarrow Cl + H_2O$
(10)	$O + CH_2O \rightarrow OH + HCO$	(54)	$HCl + O \rightarrow Cl + OH$
(11)	$H + O_2 + M \rightarrow HO_2 + M$	(55)	$Cl + O_2 + M \rightarrow ClO_2 + M$
(12)	$O_3 + OH \rightarrow HO_2 + O_2$	(56)	$ClO_2 + M \rightarrow Cl + O_2 + M$
(13)	$O_3 + NO \rightarrow NO_2 + O_2$	(57)	$HO_2 + NO_2 + M \rightarrow HO_2NO_2 + M$
(14)	$NO_2 + O_3 \rightarrow NO_3 + O_2$	(58)	$Cl + ClO_2 \rightarrow 2ClO$

Table 3. (continued)

No.	Reaction	No.	Reaction
(15)	$O_3 + H \rightarrow OH + O_2$	(59)	$Cl + ClO_2 \rightarrow Cl_2 + O_2$
(16)	$OH + OH \rightarrow H_2O + O$	(60)	$ClO + ClO + M \rightarrow Cl_2O_2 + M$
(17)	$OH + HO_2 \rightarrow H_2O + O_2$	(61)	$Cl_2O_2 + M \rightarrow 2ClO$
	$OH + HO_2 + M \rightarrow H_2O + O_2 + M$	(62)	$HO_2NO_2 + M \rightarrow HO_2 + NO_2 + M$
(18)	$OH + NO_2 + M \rightarrow HNO_3 + M$	(64)	$OH + OH + M \rightarrow H_2O_2 + M$
(19)	$OH + NO + M \rightarrow HNO_2 + M$	(65)	$H_2O_2 + O \rightarrow OH + HO_2$
(20)	$HO_2 + NO \rightarrow OH + NO_2$	(66)	$CH_4 + OH \rightarrow CH_3 + H_2O$
(21)	$OH + H_2O_2 \rightarrow H_2O + HO_2$	(67)	$ClO + NO_2 + M \rightarrow ClONO_2 + M$
(22)	$HO_2 + HO_2 \rightarrow H_2O_2 + O_2$	(68)	$ClONO_2(g) + HCl(s) \rightarrow Cl_2(g) + HNO_3(s)$
	$HO_2 + HO_2 + M \rightarrow$	(69)	$ClONO_2 + O \rightarrow \text{products}$
	$H_2O_2 + O_2 + M$	(70)	$HO_2NO_2 + OH \rightarrow \text{products}$
(23)	$NO + NO_3 \rightarrow 2NO_2$	(71)	$HCl + O(^1D) \rightarrow Cl + OH$
(24)	$NO + O + M \rightarrow NO_2 + M$	(72)	$H_2 + OH \rightarrow H_2O + H$
(25)	$N_2O + O(^1D) \rightarrow N_2 + O_2$	(73)	$ClONO_2(g) + H_2O(s) \rightarrow HOCl(g) + HNO_3(s)$
(26)	$N_2O + O(^1D) \rightarrow 2NO$	(74)	$CF_2Cl_2 + O(^1D) \rightarrow 2Cl + \dots$
(27)	$N_2 + O(^1D) + M \rightarrow N_2O + M$	(75)	$CFCl_3 + O(^1D) \rightarrow 3Cl + \dots$
(28)	$HO_2 + O_3 \rightarrow OH + 2O_2$	(76)	$N_2O_5(s) + HCl(s) \rightarrow ClNO_2(g) + HNO_3(s)$
(29)	$HNO_3 + OH \rightarrow H_2O + NO_3$	(77)	$CH_3 + O_2 + M \rightarrow CH_3O_2 + M$
(30)	$H_2 + O(^1D) \rightarrow H + OH$	(78)	$CH_3O_2 + HO_2 \rightarrow CH_3OOH + O_2$
(31)	$CH_3CCl_3 + OH \rightarrow 3Cl + \dots$	(79)	$CH_3O_2 + NO \rightarrow CH_3O + NO_2$
(32)	$CH_4 + O(^1D) \rightarrow CH_3 + OH$	(80)	$N_2O_5(g) + H_2O(s) \rightarrow 2HNO_3(s)$
(33)	$ClO + HO_2 \rightarrow HOCl + O_2$	(81)	$ClO + OH \rightarrow HCl + O_2$
(34)	$NO_2 + O + M \rightarrow NO_3 + M$		$ClO + OH \rightarrow Cl + HO_2$
(35)	$NO_2 + NO_3 + M \rightarrow N_2O_5 + M$	(82)	$CH_3O + O_2 \rightarrow CH_2O + HO_2$
(36)	$N_2O_5 + M \rightarrow NO_2 + NO_3 + M$	(83)	$CH_2O + OH \rightarrow HCO + H_2O$
(39)	$N + NO_2 \rightarrow N_2O + O$	(84)	$HCO + O_2 \rightarrow CO + HO_2$
(40)	$N + O_2 \rightarrow NO + O$	(85)	$CO + OH \rightarrow H + CO_2$
(41)	$N + NO \rightarrow N_2 + O$	(86)	$CH_3Cl + OH \rightarrow Cl + \dots$
(42)	$HOCl + O \rightarrow OH + ClO$	(87)	$CH_3OOH + OH \rightarrow CH_3O_2 + H_2O$

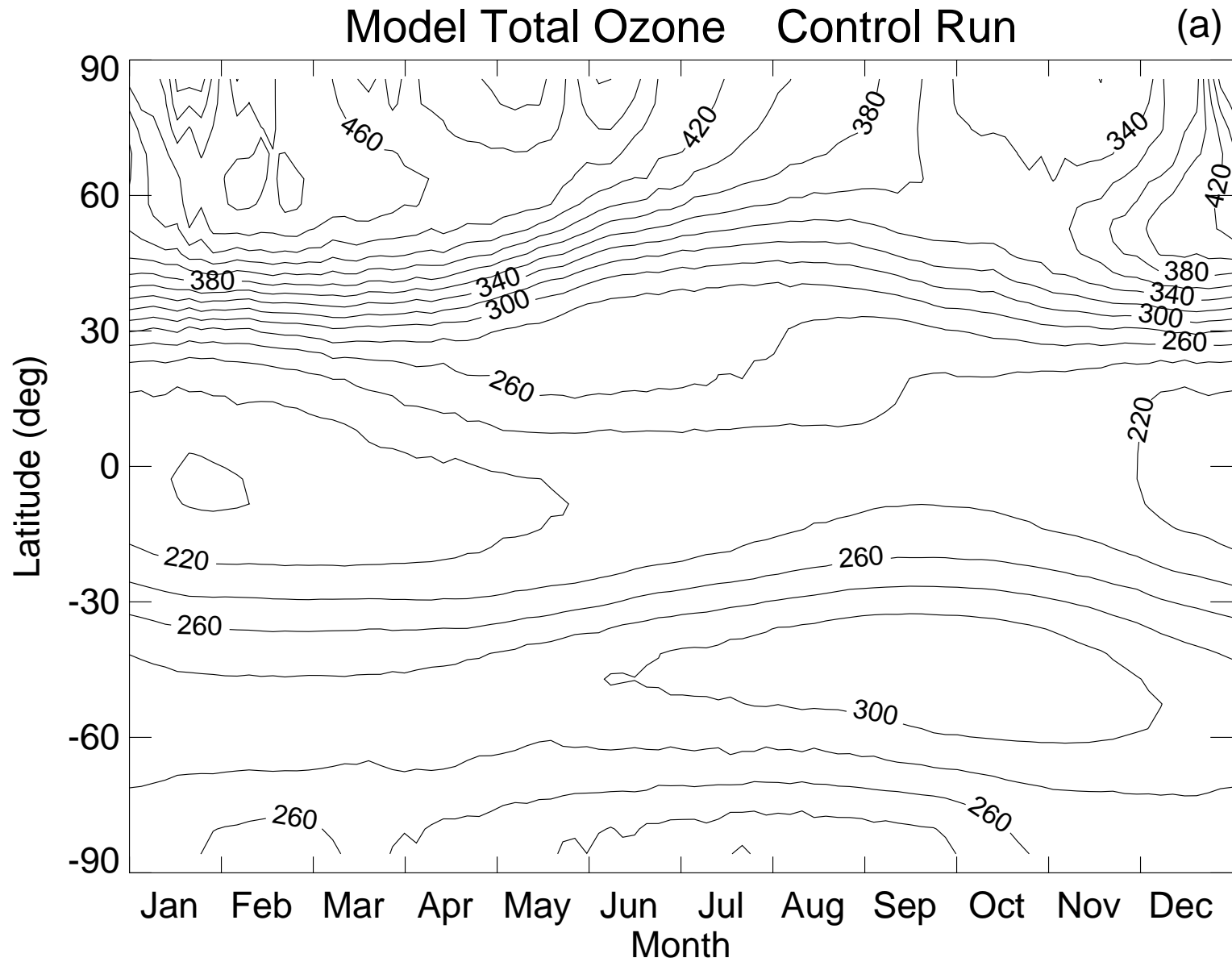


Figure 1a

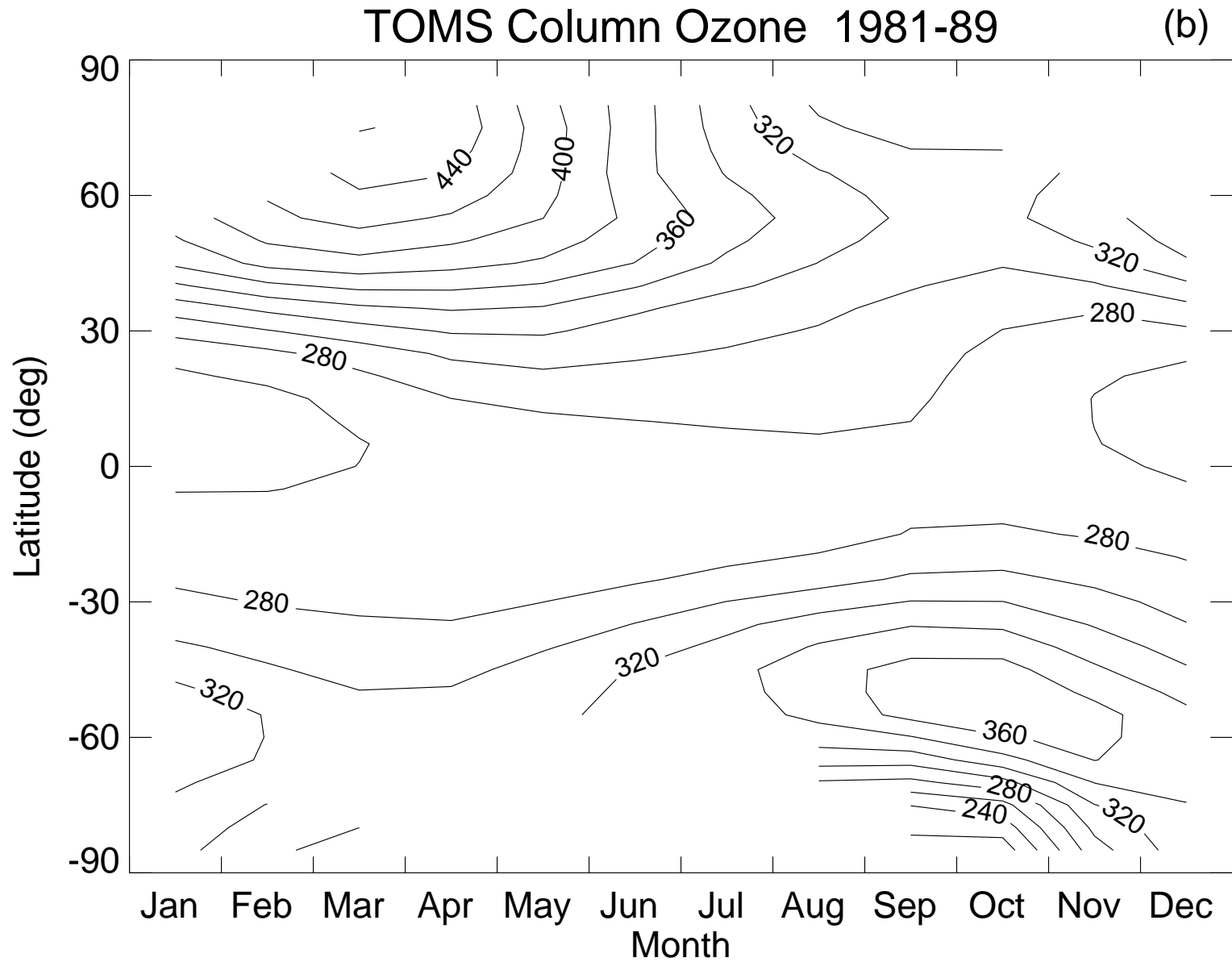


Figure 1b

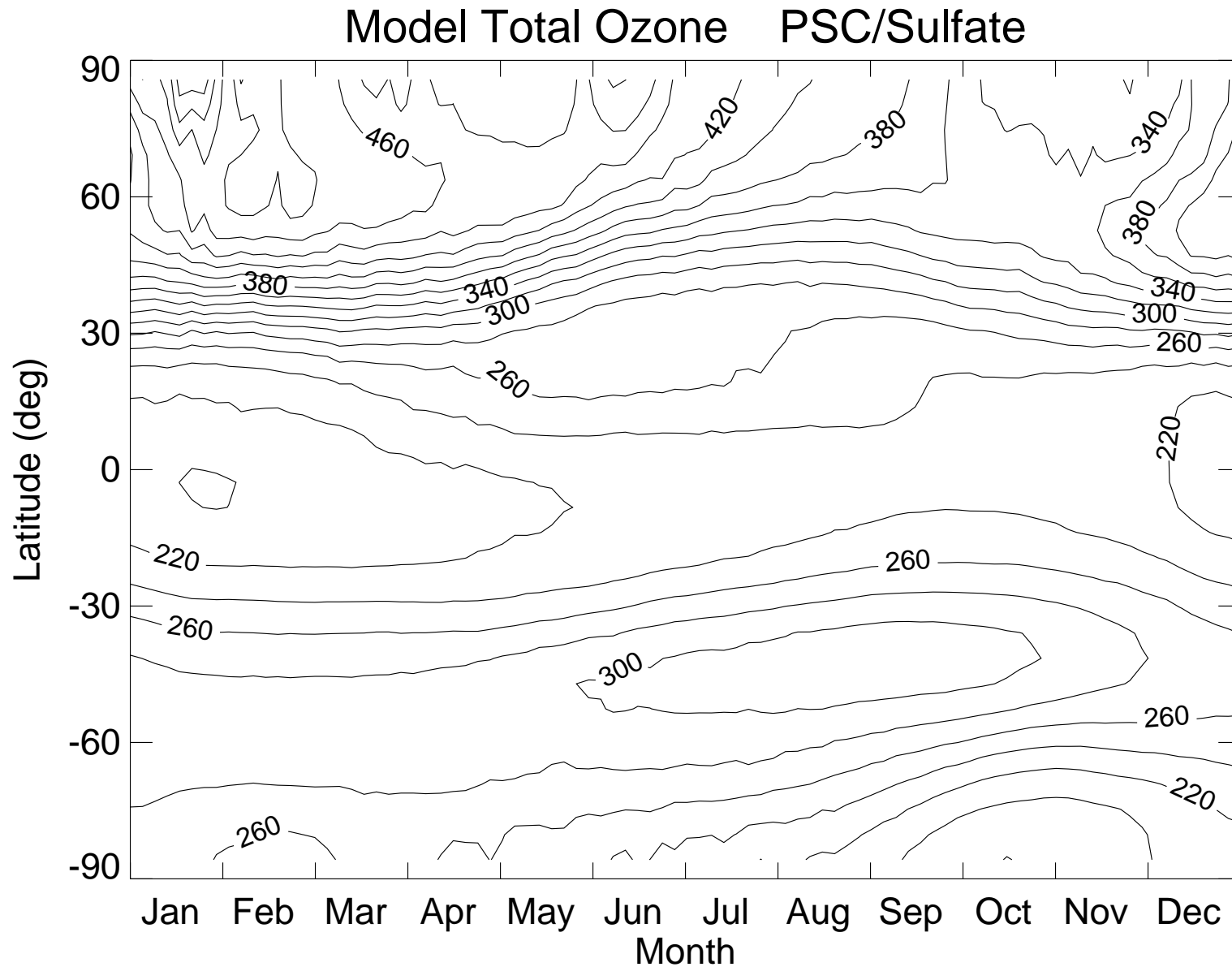


Figure 2

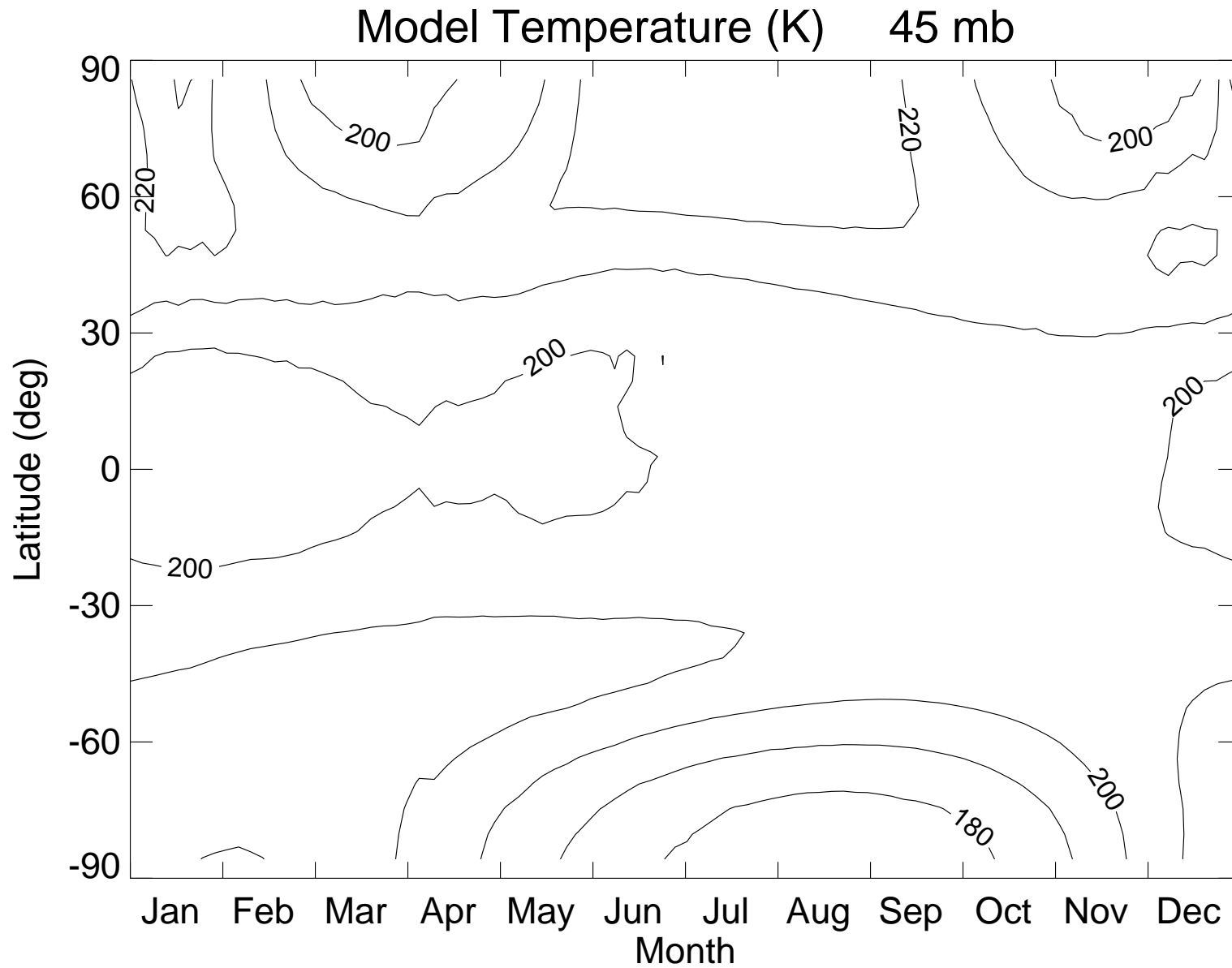


Figure 3

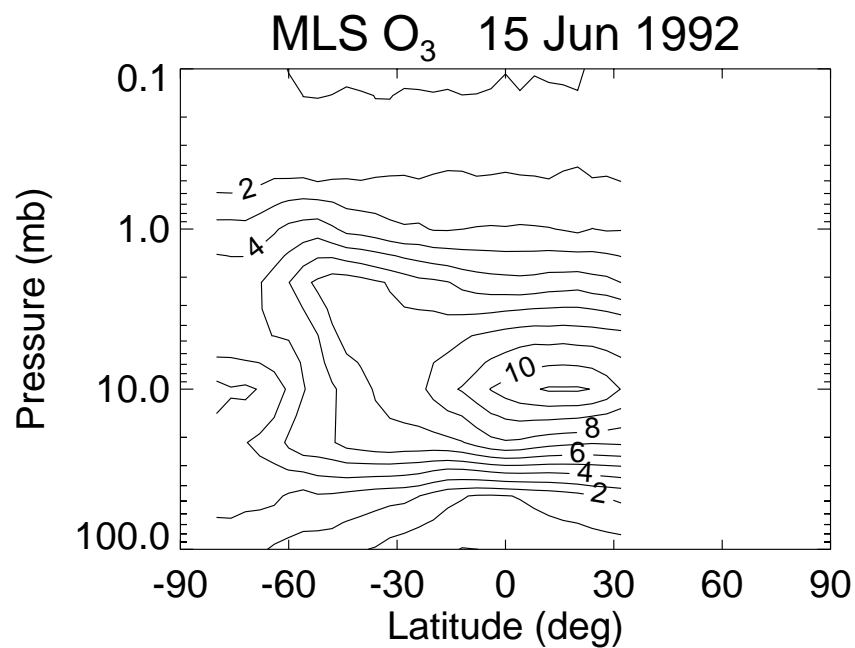
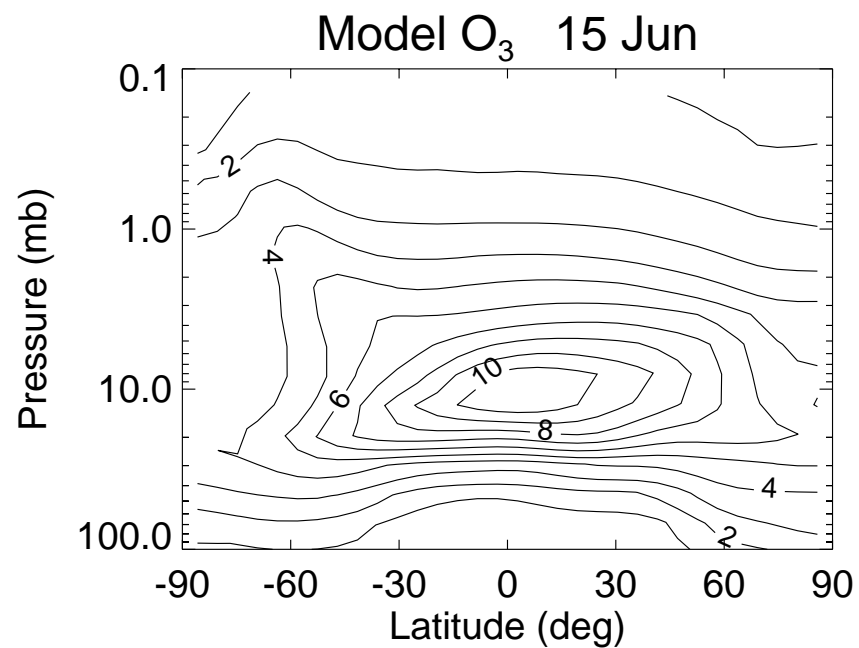
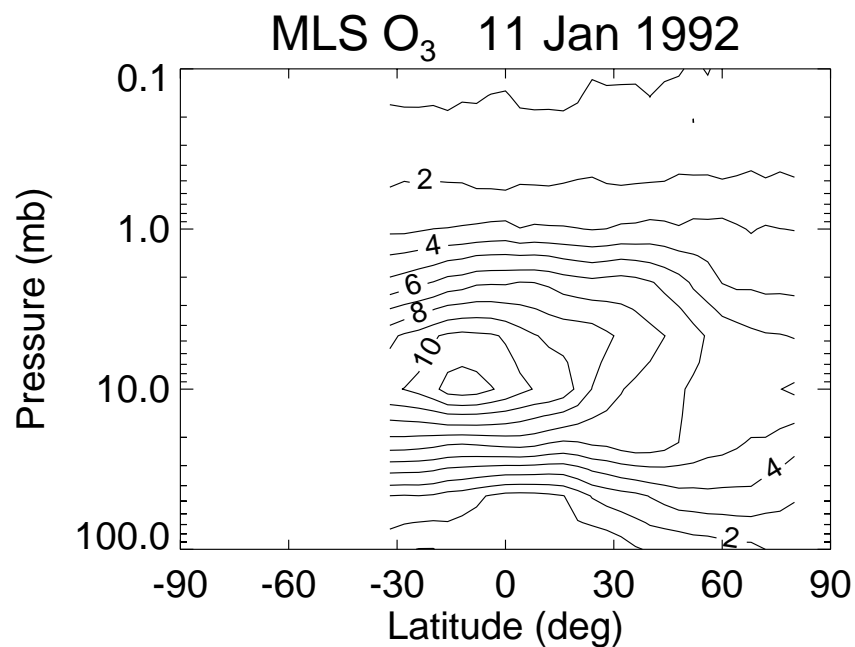
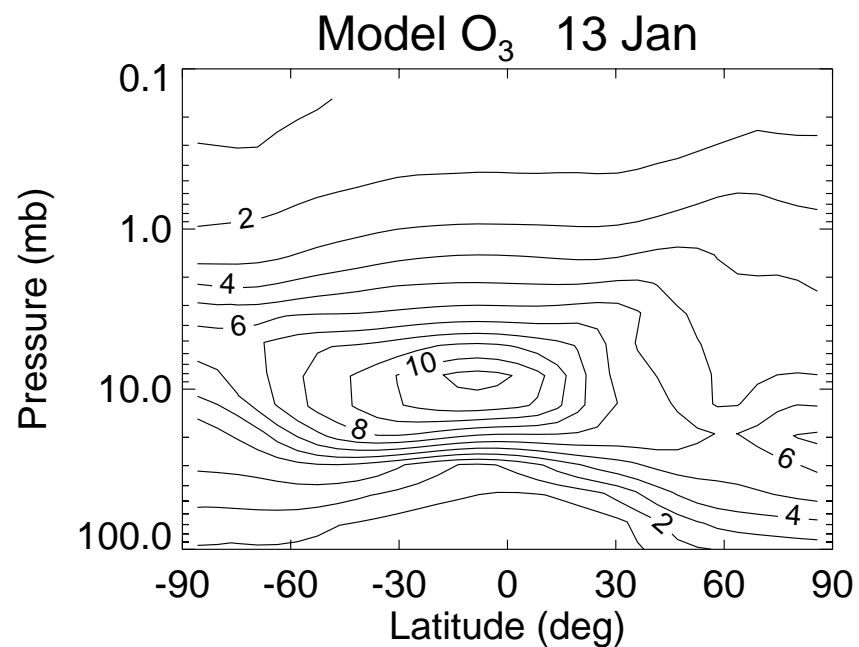


Figure 4

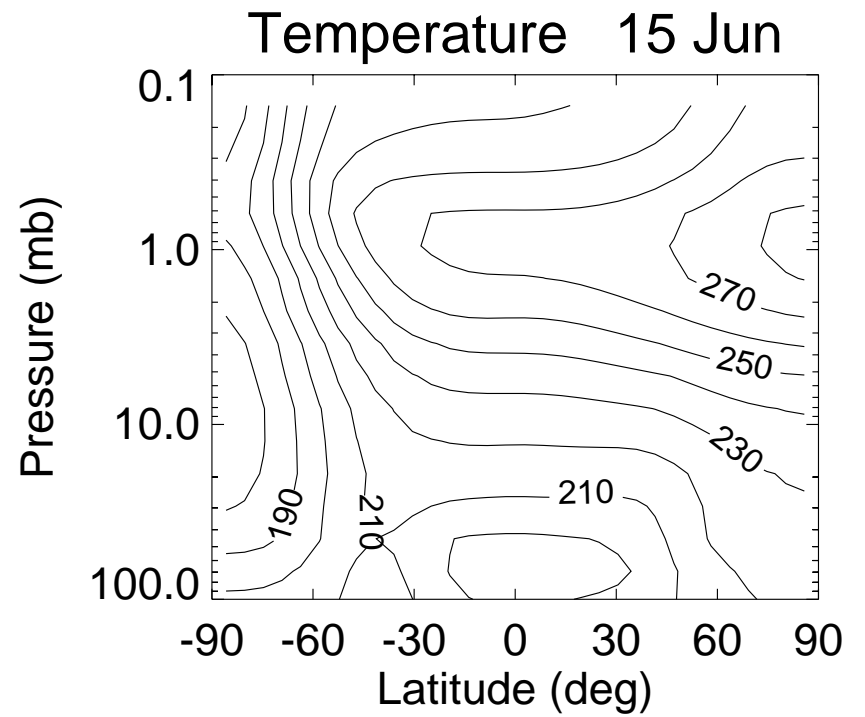
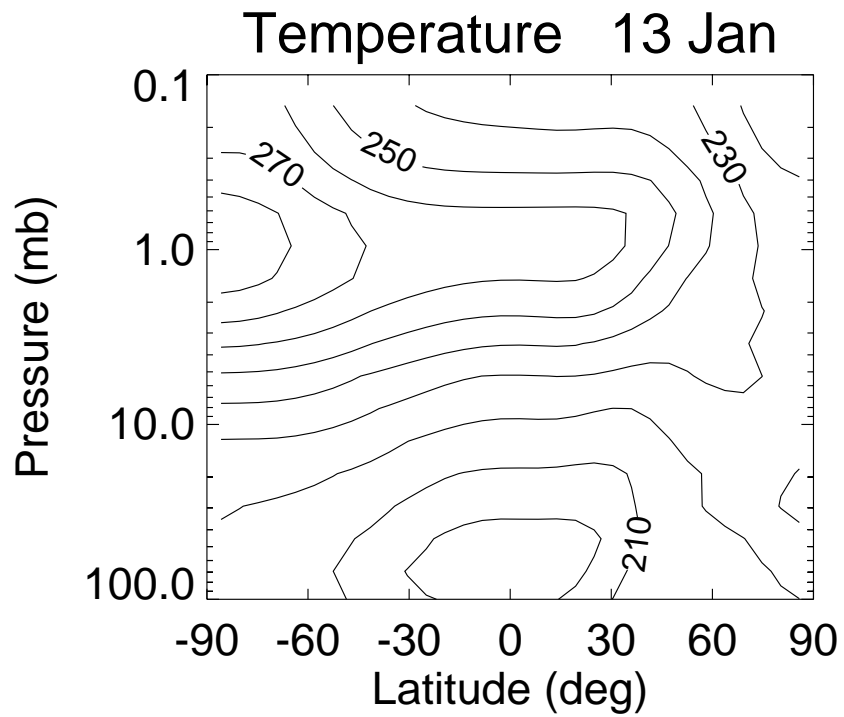


Figure 5

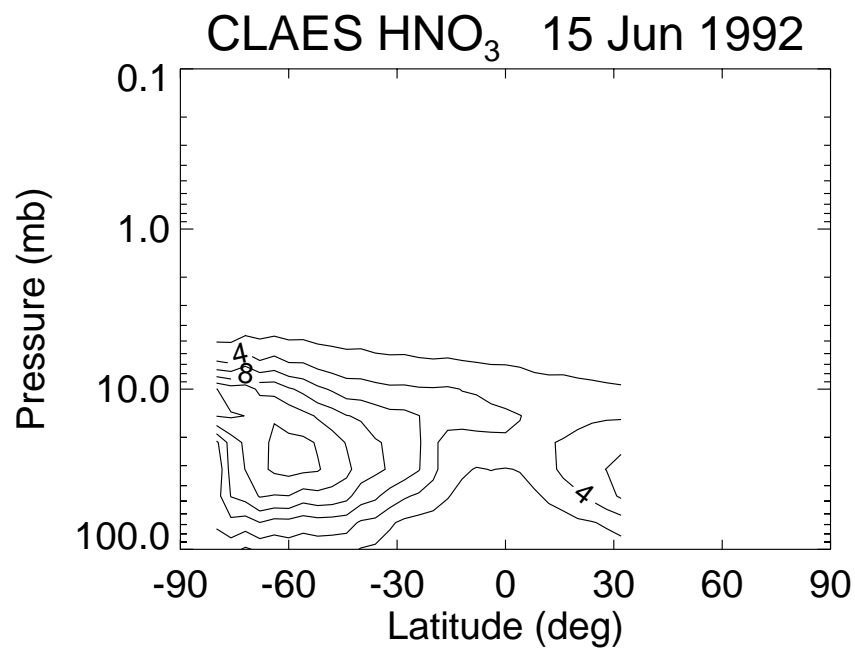
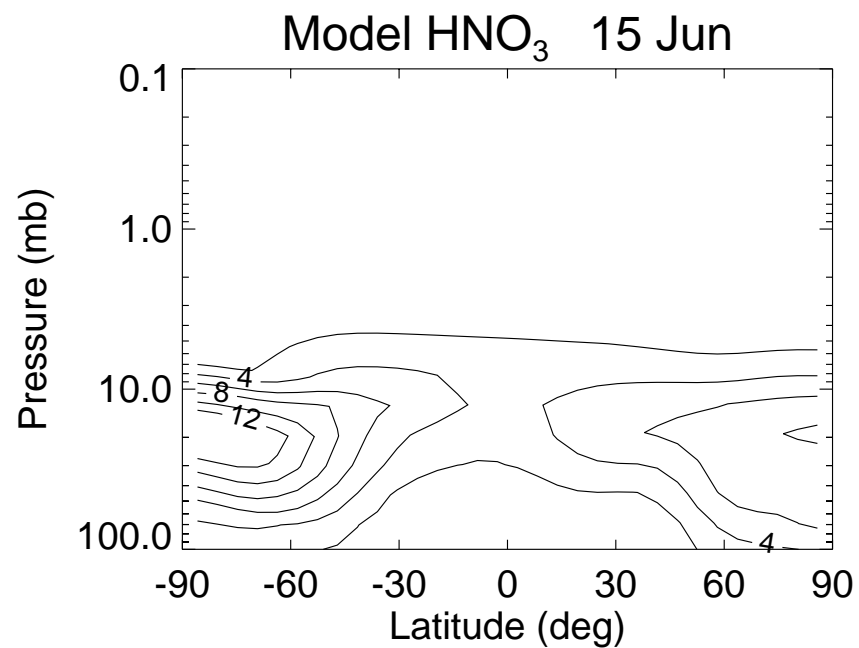
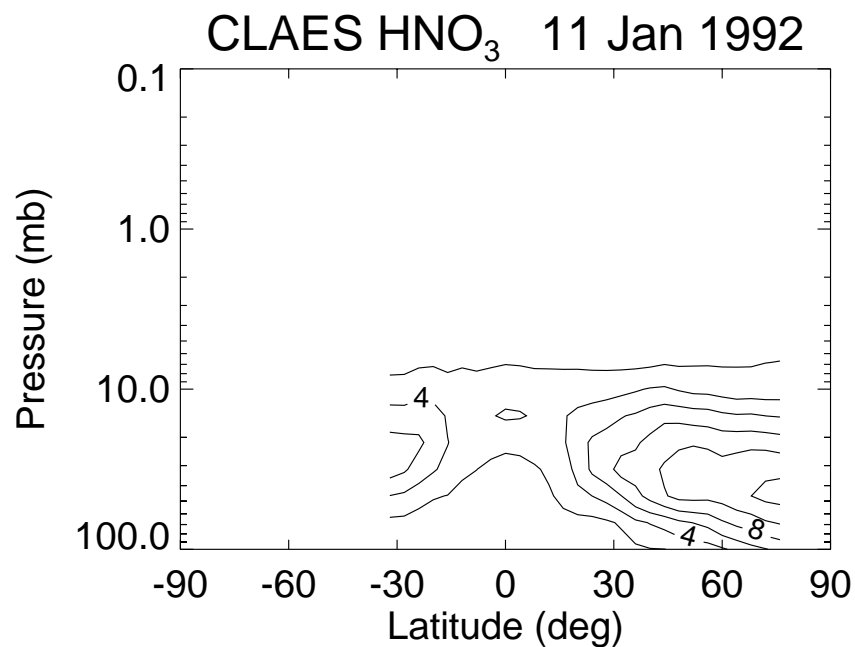
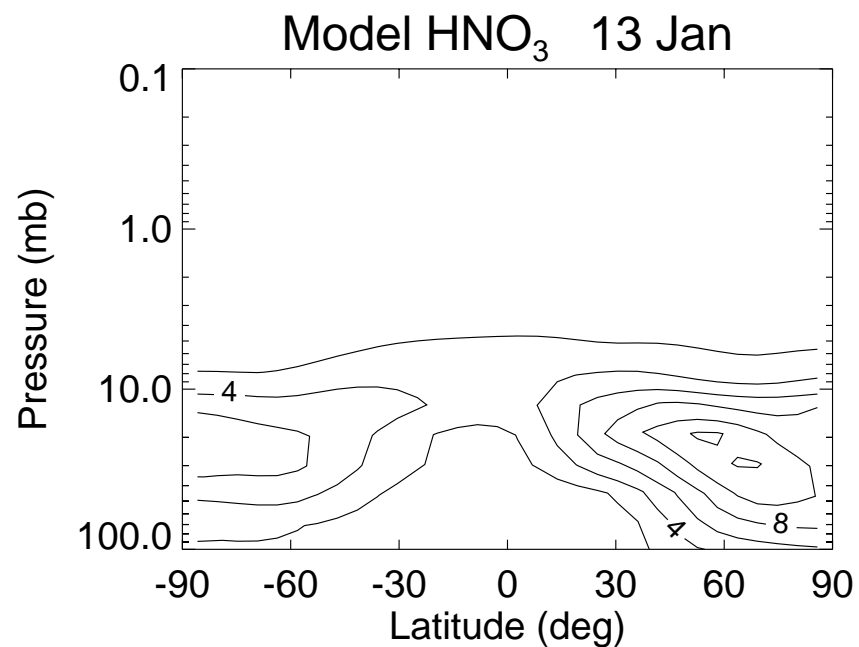


Figure 6

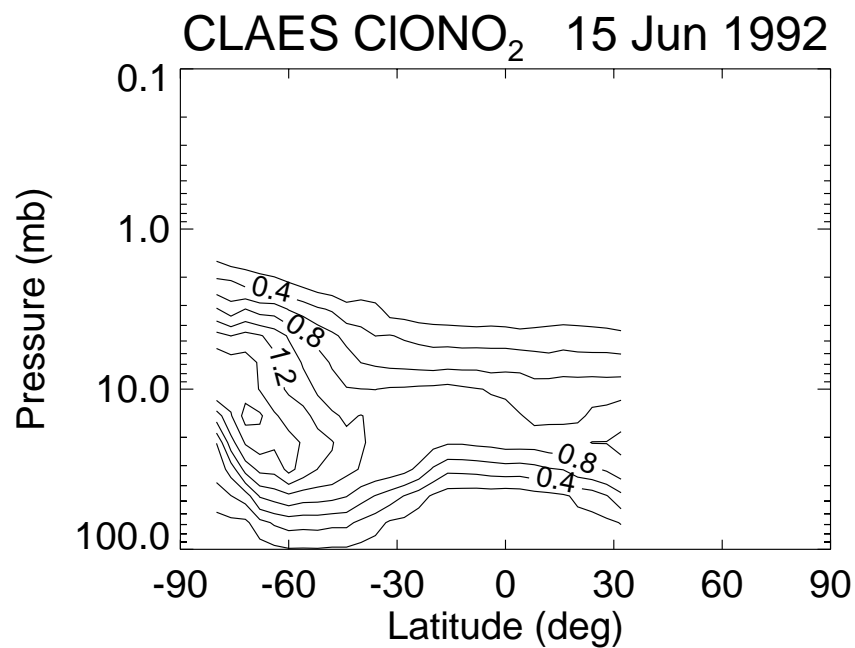
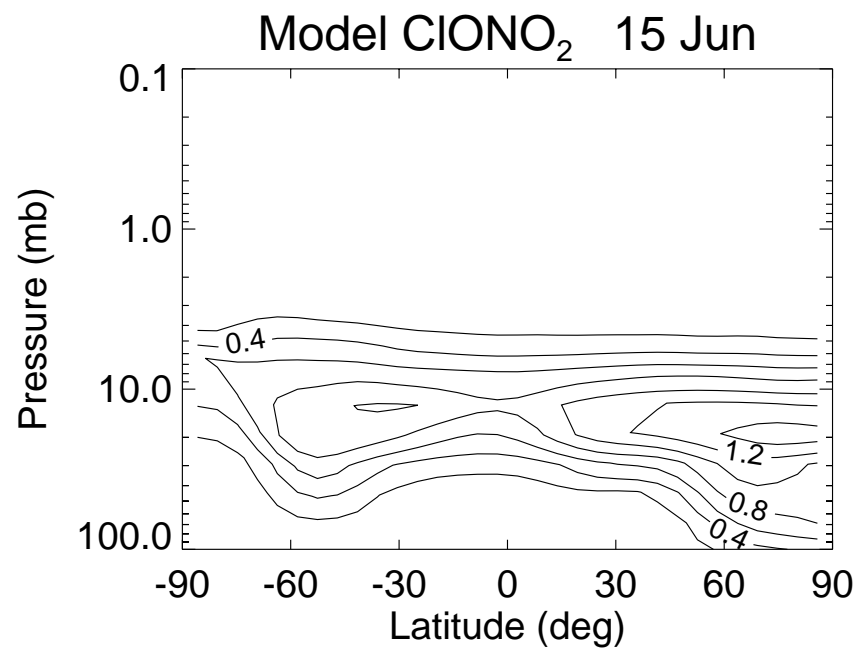
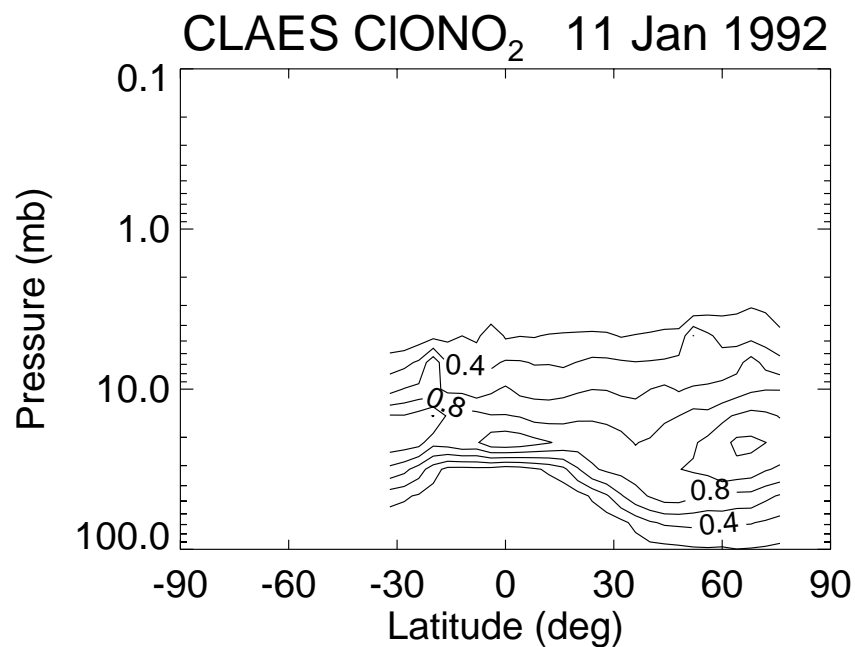
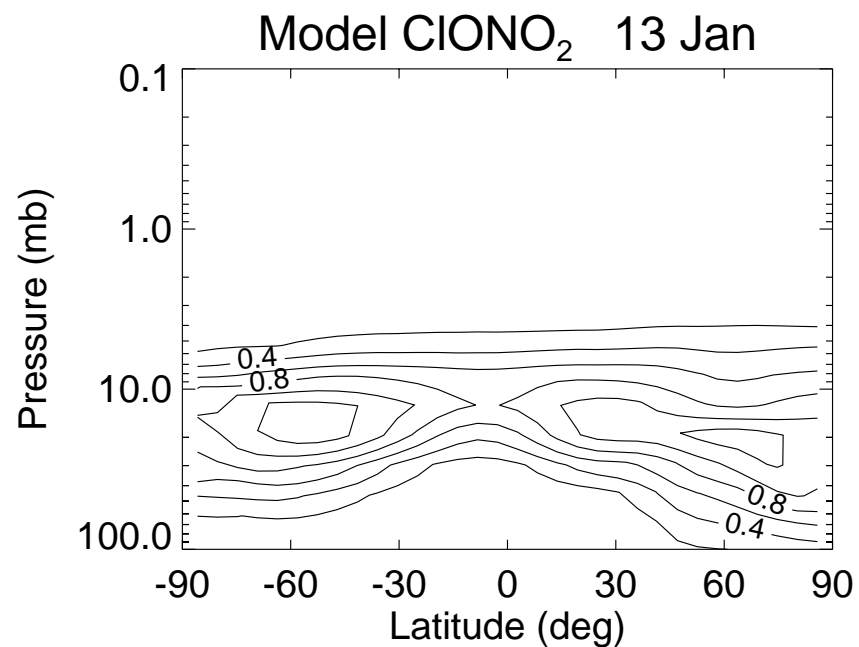


Figure 7

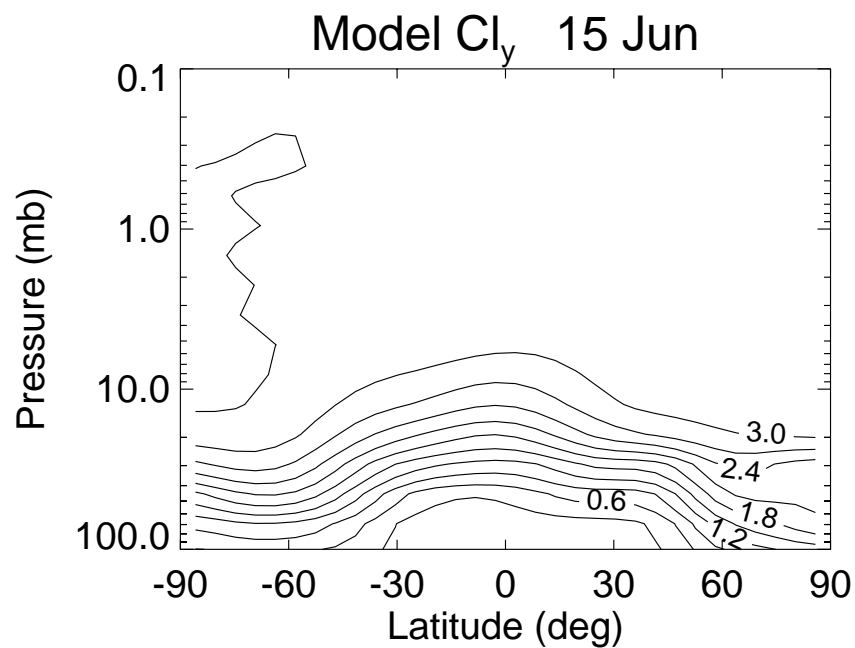
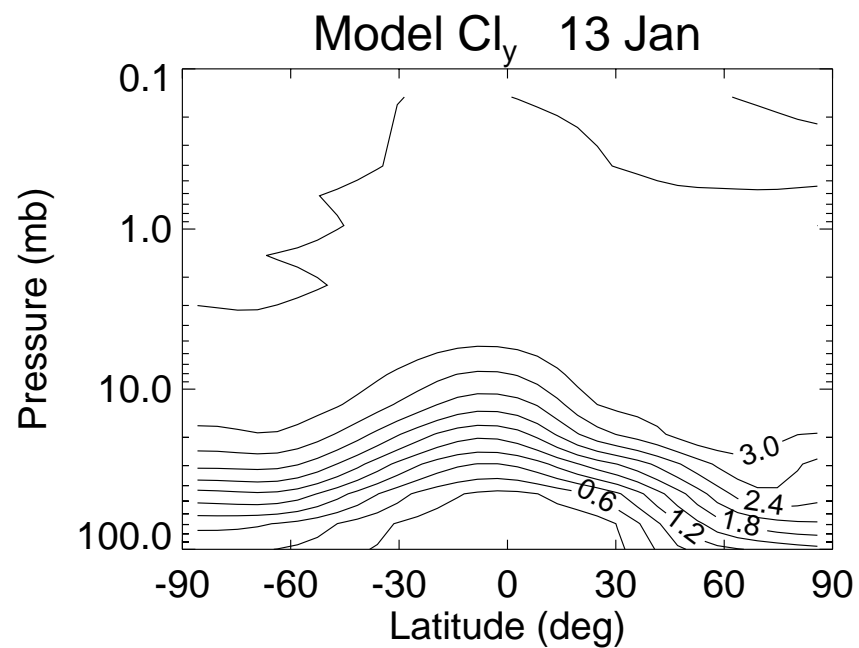
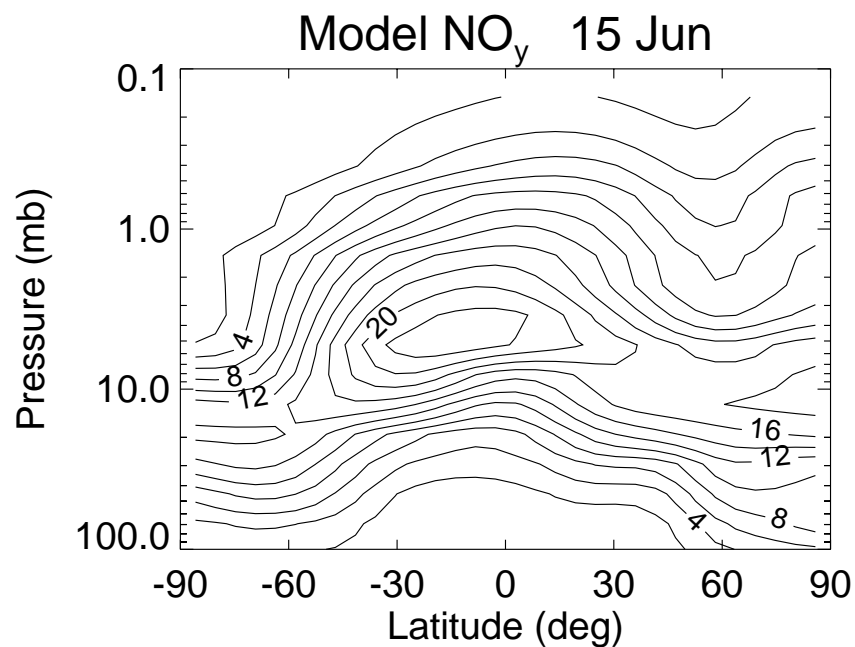
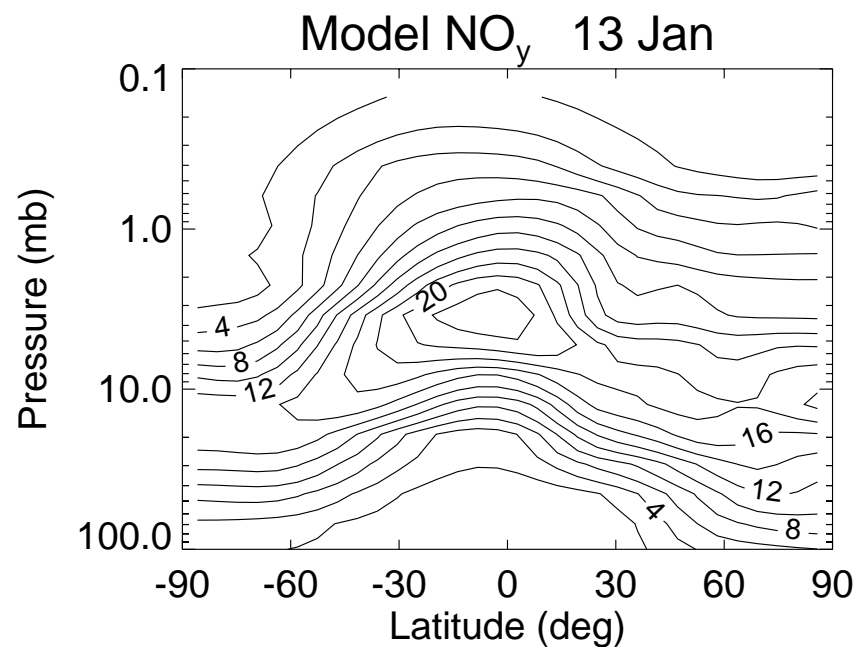


Figure 8

Normalized Potential Vorticity

September 14

$\theta=450\text{K}$

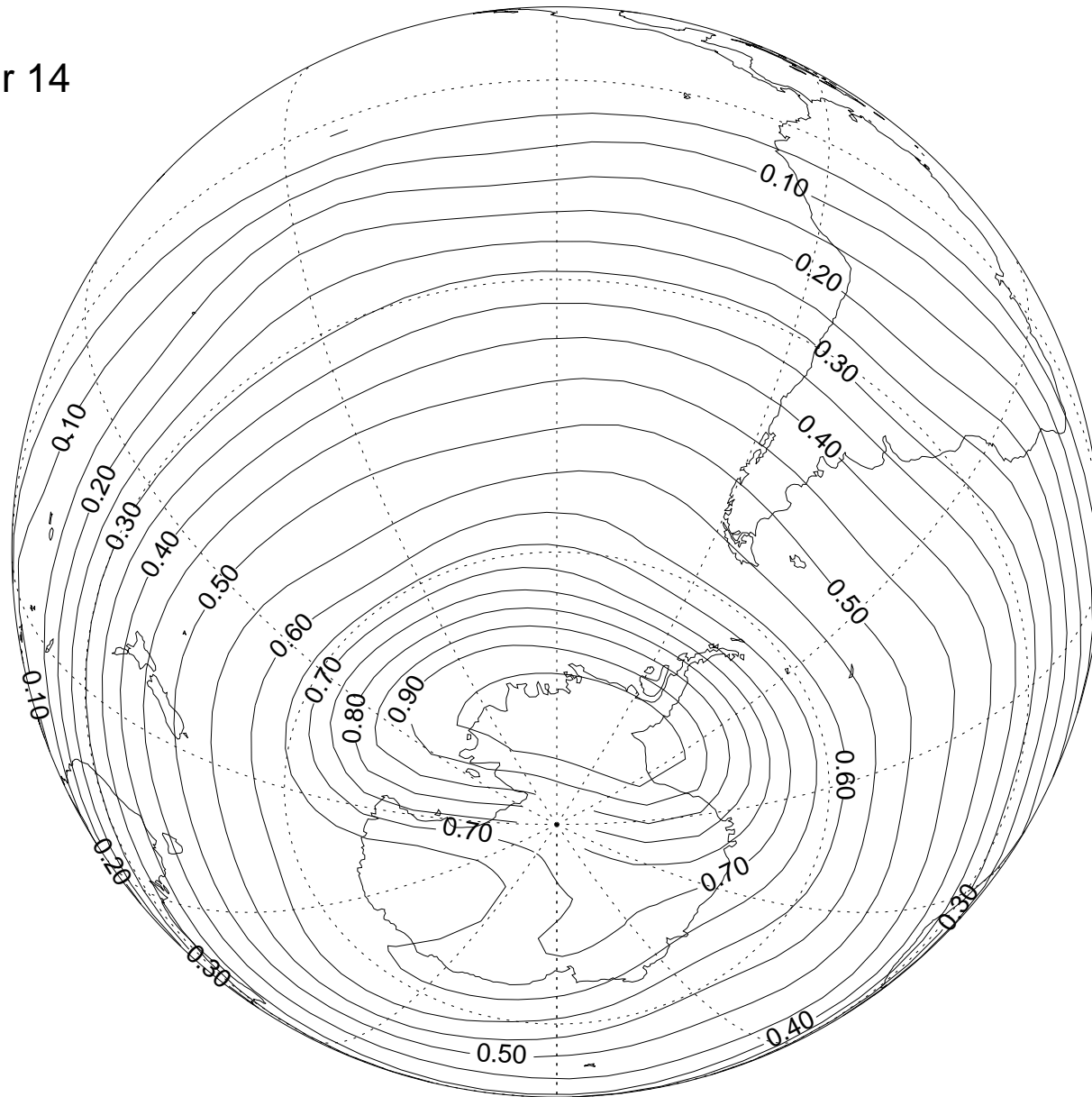


Figure 9

Model Temperature

September 14
45 mb

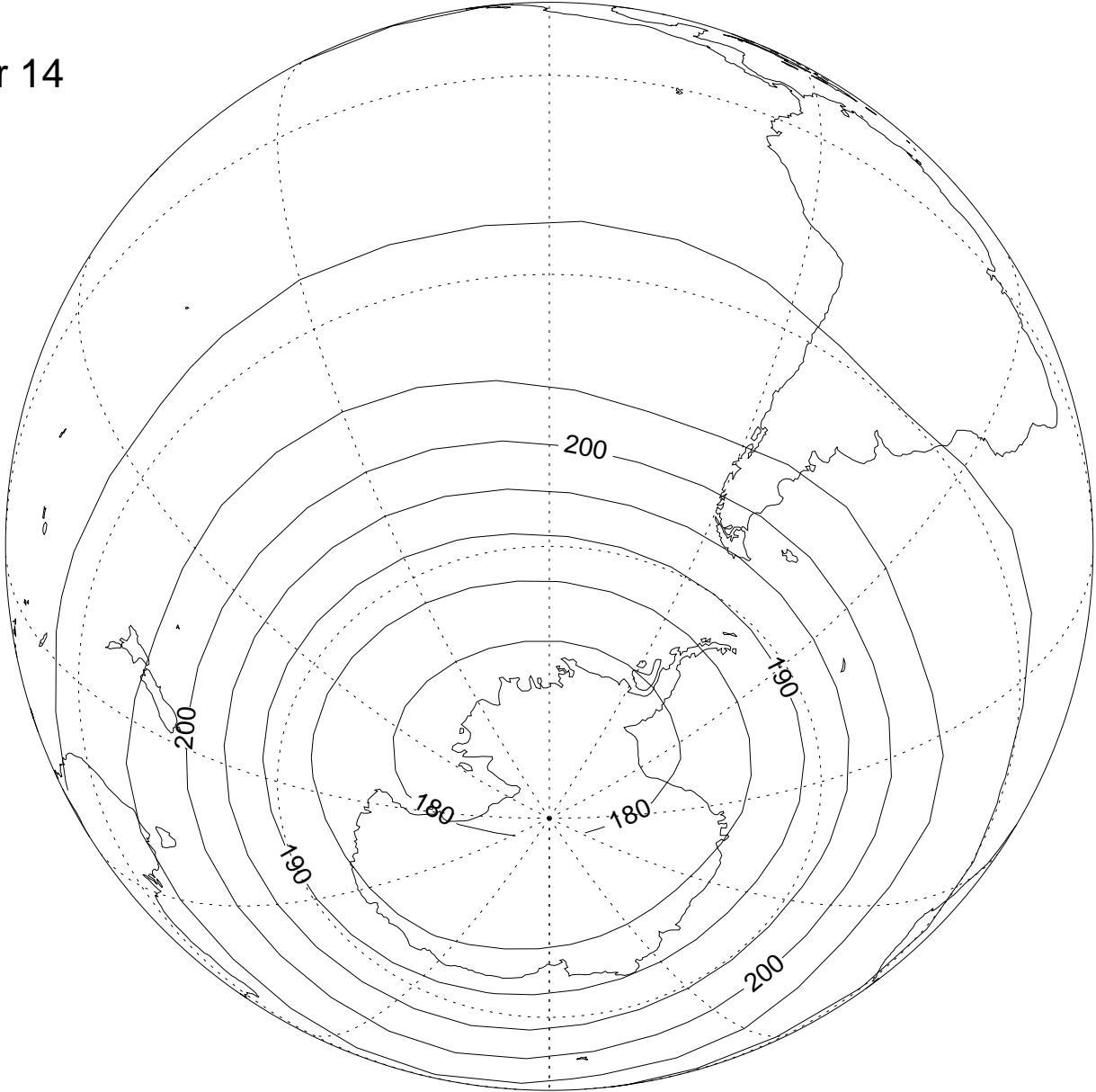


Figure 10

Model NAT

September 14
45 mb
PSC+Sulfate

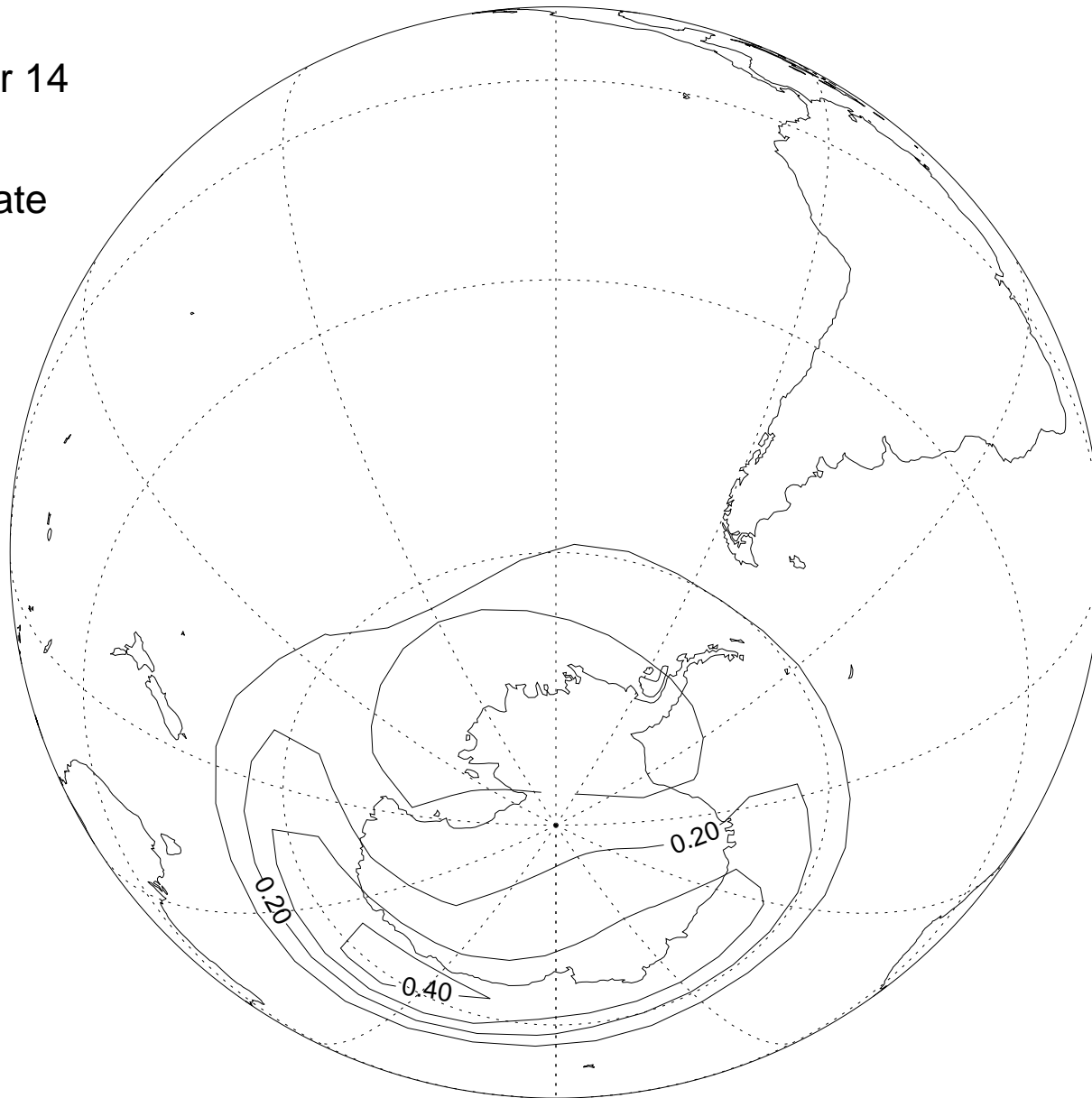


Figure 11

Model CIO

September 14
45 mb
PSC+Sulfate

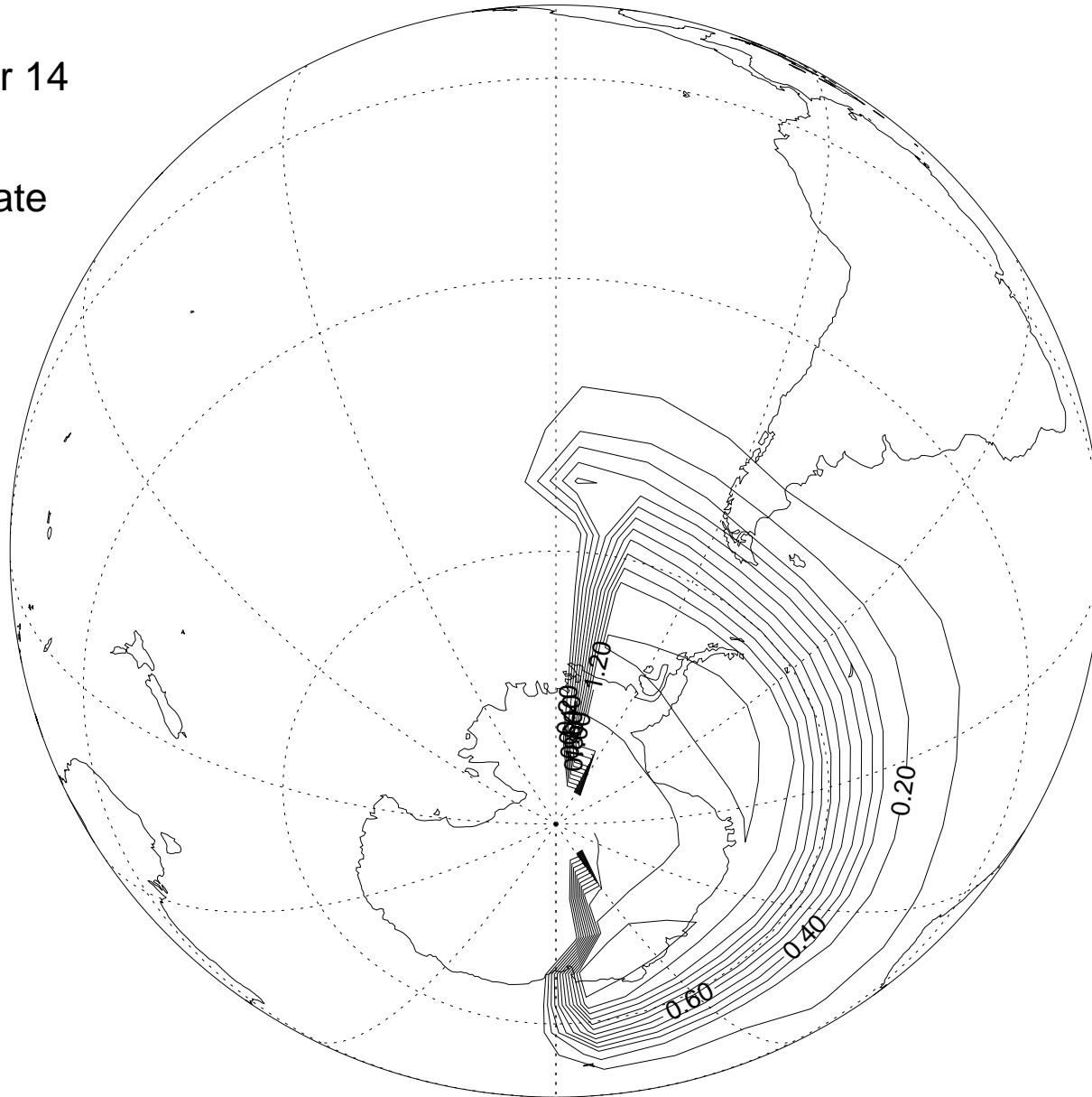


Figure 12

Model Cl_2O_2

September 14

45 mb

PSC+Sulfate

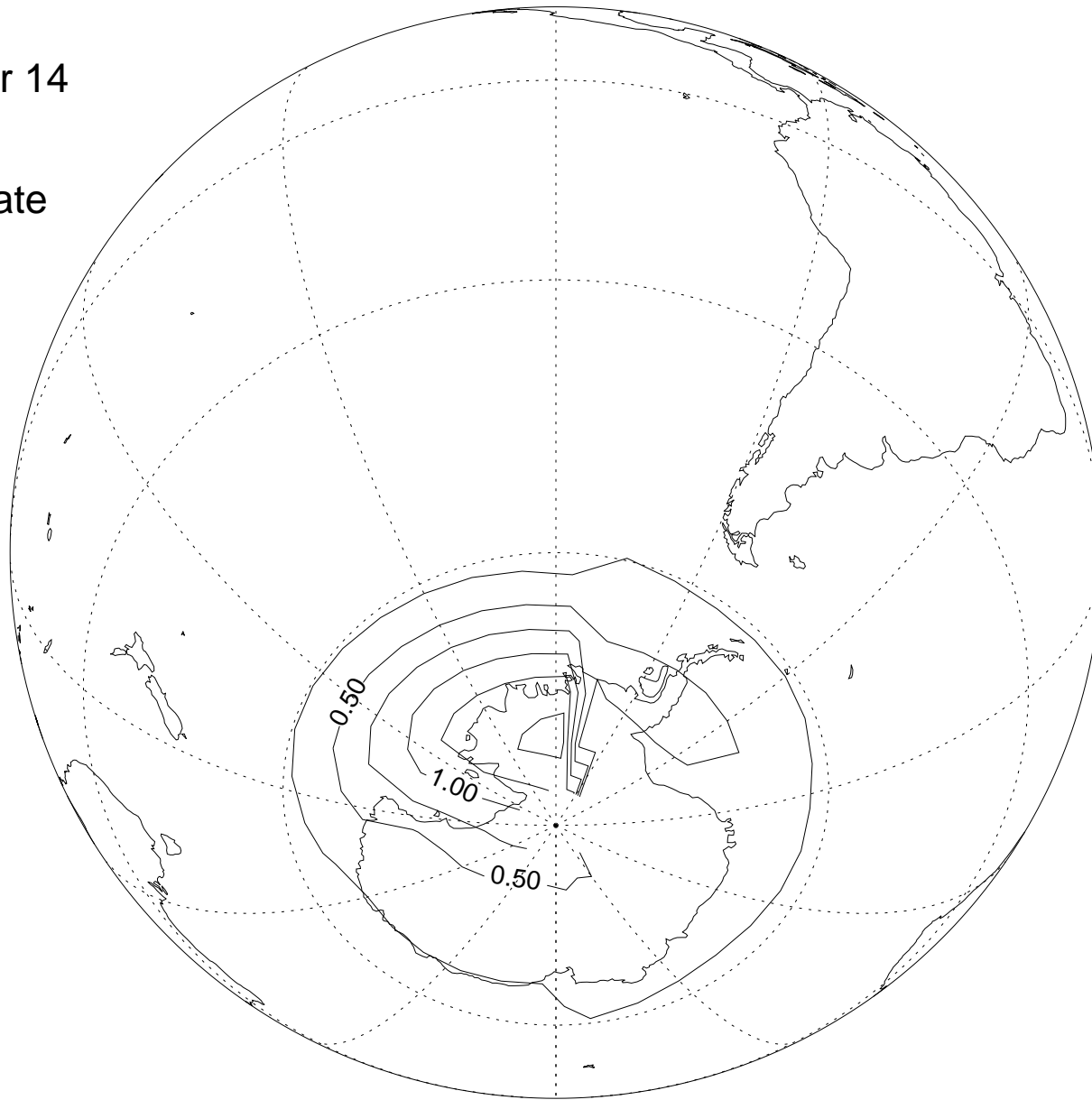


Figure 13

Model ClONO₂

September 14
45 mb
PSC+Sulfate

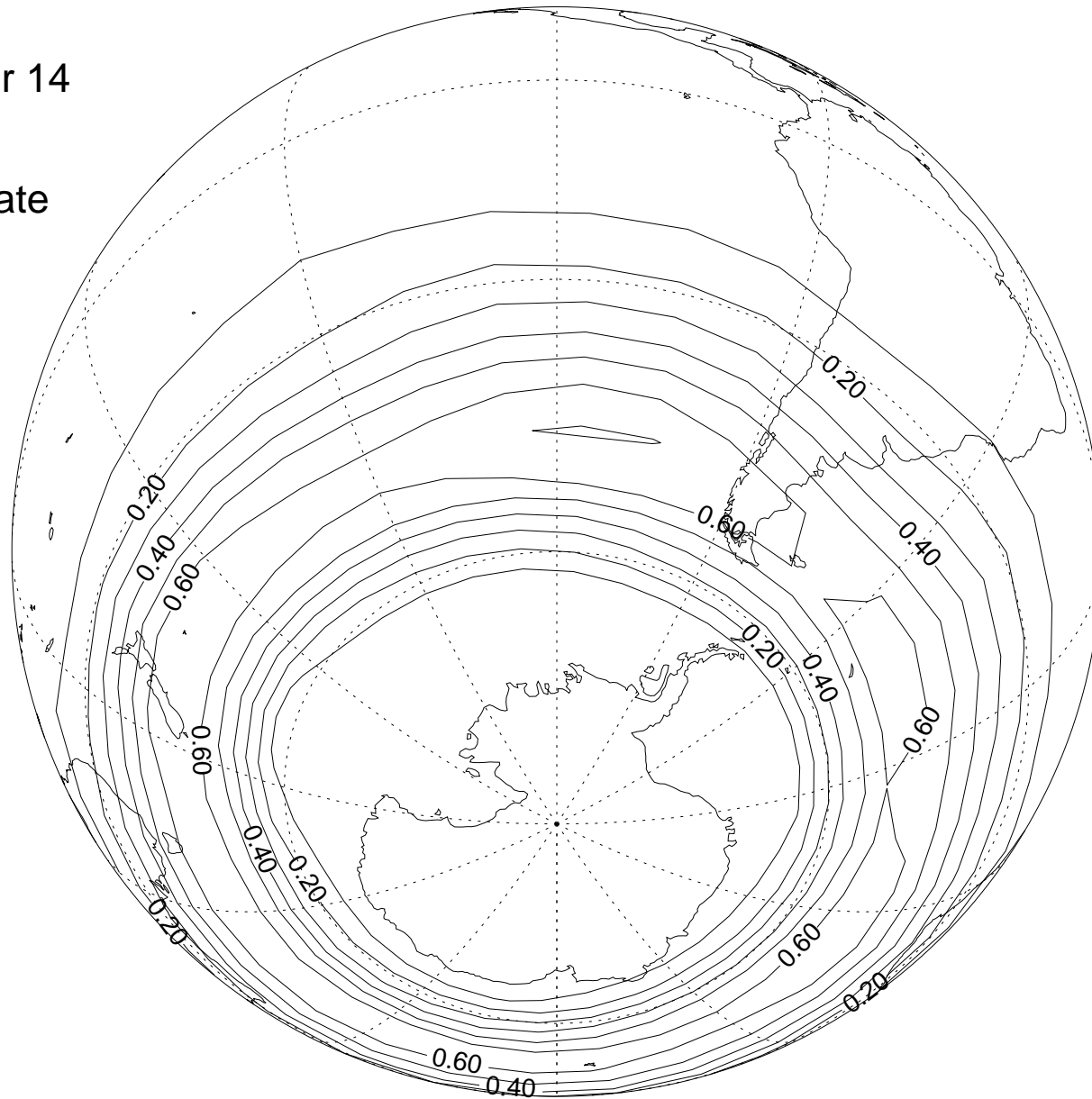


Figure 14

Model ClONO₂

September 14

45 mb

PSC only

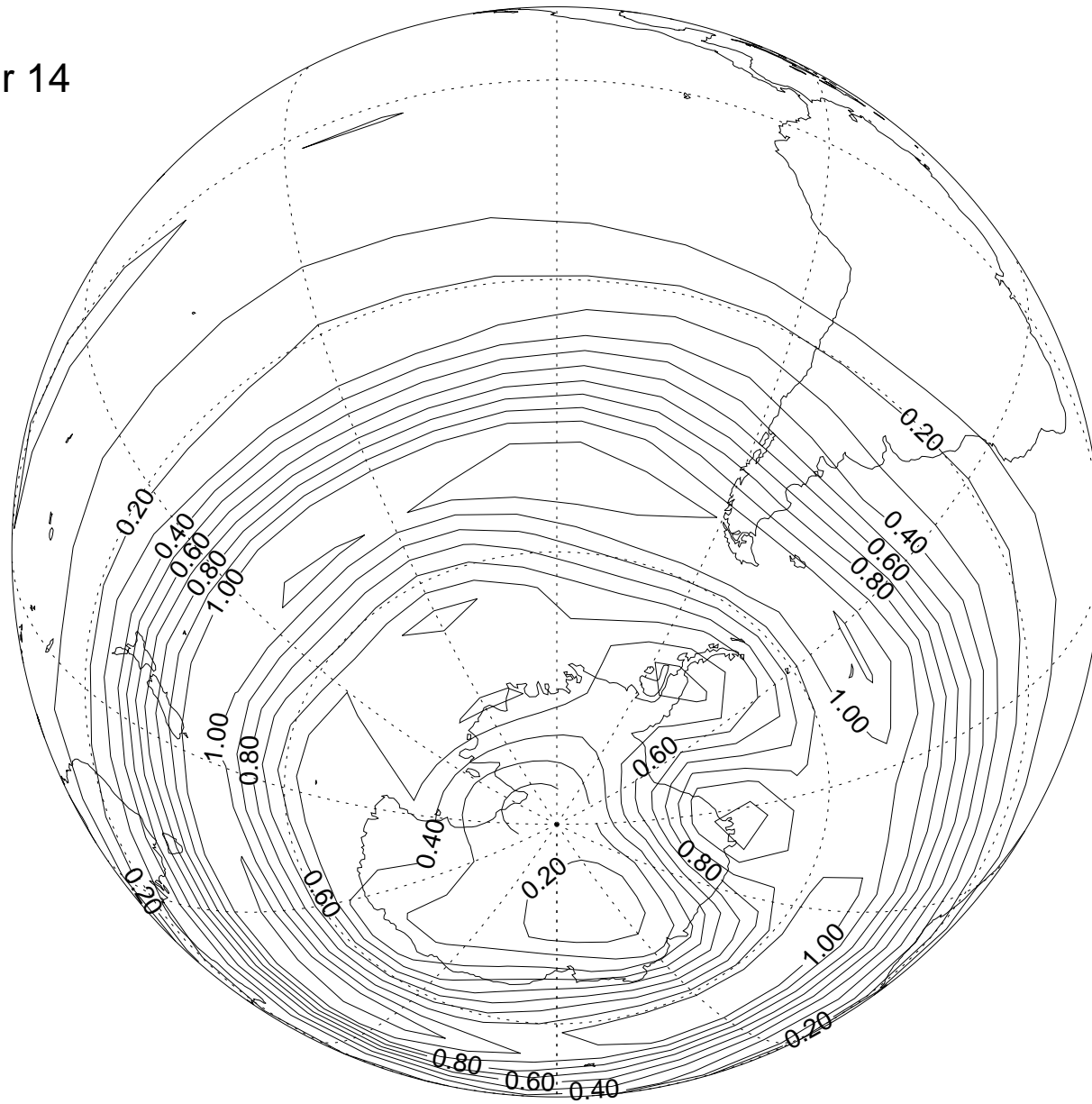


Figure 15

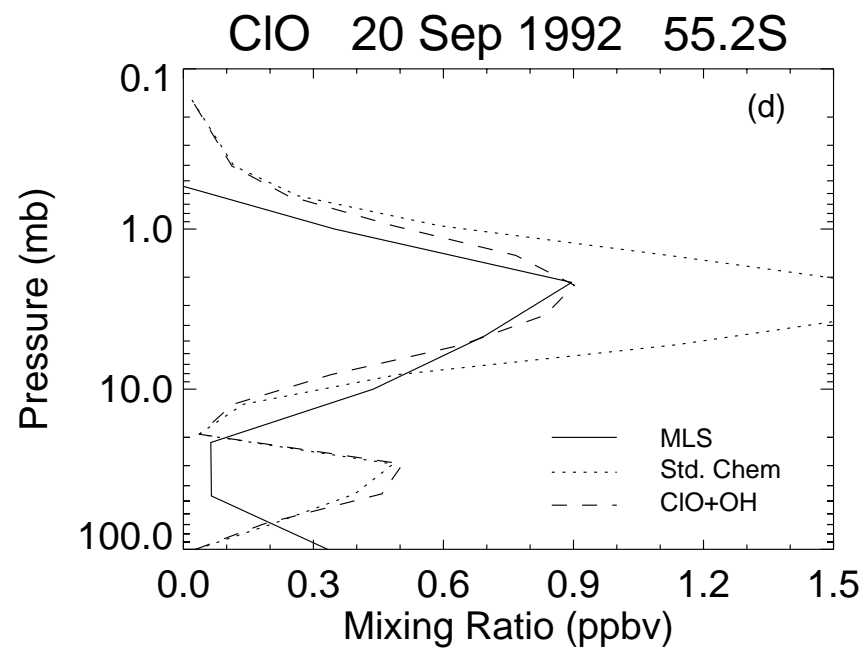
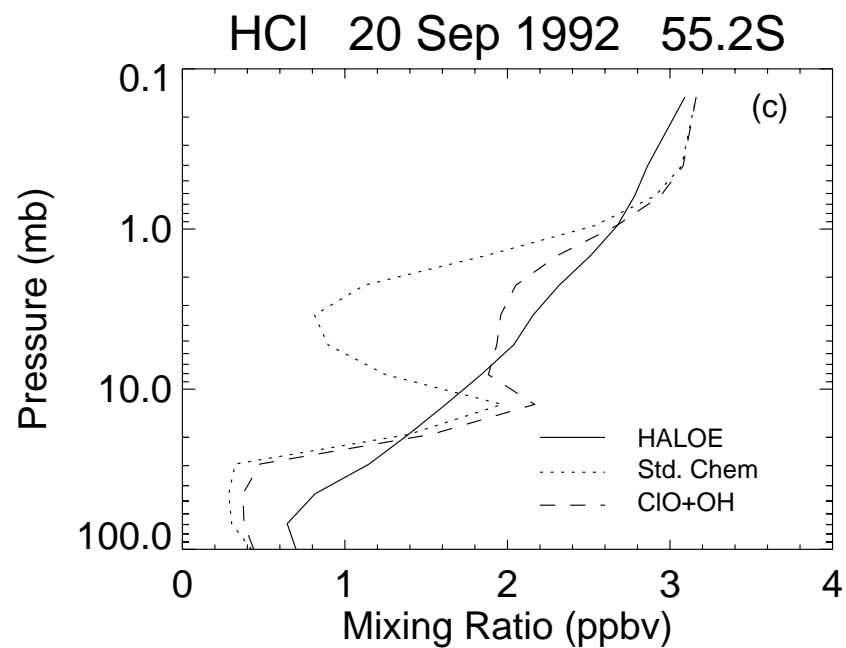
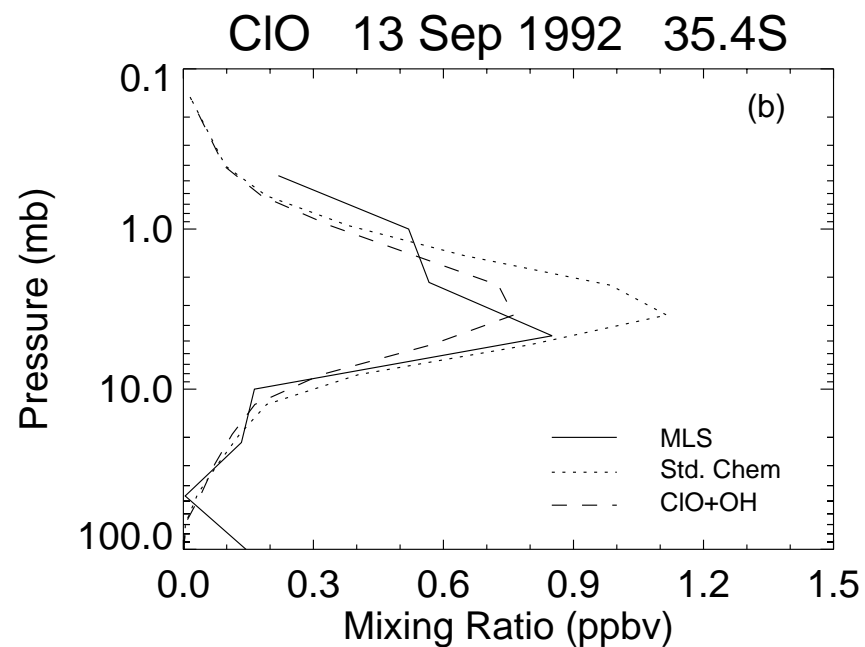
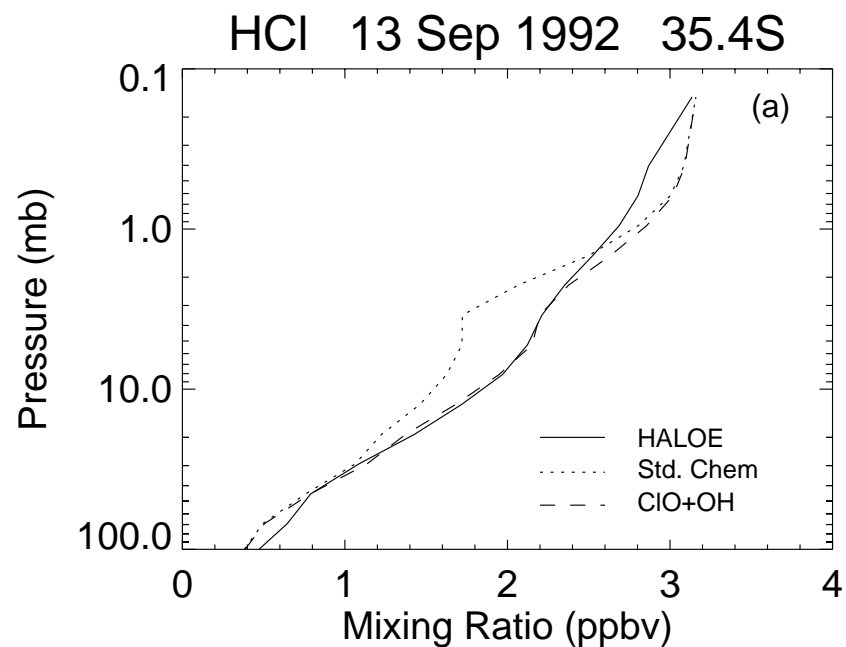


Figure 16

